Numerical Analysis of the Melt Pool Kinetics in Selective Laser Melting Based Additive Manufacturing of Mg_2Si Thermoelectric Powders

Jagannath Suresh

Dissertation submitted to the Faculty of the
Virginia Polytechnic Institute and State University
in partial fulfillment of the requirements for the degree of

Master of Science
in
Mechanical Engineering

Lei Zuo, Chair
Hang Yu
Jiangtao Cheng

December 12, 2023
Blacksburg, Virginia

Keywords: Additive Manufacturing, Thermoelectrics, Computational Fluid Dynamics, Phase Field

Numerical Analysis of the Melt Pool Kinetics in Selective Laser Melting Based Additive Manufacturing of Mg_2Si Thermoelectric Powders

Jagannath Suresh

(ABSTRACT)

Thermoelectric generators convert heat energy to electricity and can be used for waste heat recovery, enabling sustainable development. Selective Laser Melting (SLM) based additive manufacturing process is a scalable and flexible method that has shown promising results in manufacturing high ZT Bi_2Te_3 material and is possible to be extended to other material classes such as Mg_2Si. The physical phenomena of melting and solidification were investigated for SLM-based manufacturing of thermoelectric (Mg_2Si) powders through comprehensive numerical models developed in MATLAB. In this study, Computational Fluid Dynamics (CFD)-based techniques were employed to solve conservation equations, enabling a detailed understanding of thermofluid dynamics, including the temperature evolution and the convection currents of the liquid melt within the molten pool. This approach was critical for optimizing processing parameters in our investigation, which were also used for printing the Mg_2Si powders using SLM. Additionally, a phase field-based model was developed to simulate the directional solidification of the Mg_2Si in MATLAB. Microstructural parameters like the Secondary and Primary Dendritic Arm Spacing were studied to correlate the effects of processing parameters to the microstructure of Mg_2Si.

Numerical Analysis of the Melt Pool Kinetics in Selective Laser Melting Based Additive Manufacturing of Mg_2Si Thermoelectric Powders

Jagannath Suresh

(GENERAL AUDIENCE ABSTRACT)

Thermoelectric generators are devices that transform heat energy into electricity, offering a way to capture and utilize waste heat for sustainable purposes. A cutting-edge manufacturing method called Selective Laser Melting (SLM) has shown great potential in creating high-performance materials like Bi_2Te_3 for thermoelectric applications. Researchers are now exploring the extension of this technique to other materials, such as Mg_2Si. This study delves into the intricate process of melting and solidifying Mg_2Si powders using SLM. Advanced computer models were created in MATLAB, to simulate these processes in detail. By employing Computational Fluid Dynamics (CFD) techniques, heat and fluid flow within the molten material was also closely examined. These simulations were vital for fine-tuning the printing settings used to fabricate Mg_2Si powders via SLM. Moreover, a specialized model based on phase field theory was developed to mimic the solidification of Mg_2Si. The effects of changing manufacturing parameters on the microstructure of the final product were examined. Understanding these microstructural aspects is crucial for optimizing the manufacturing process and ultimately enhancing the performance of Mg_2Si for thermoelectric applications.

Acknowledgments

I am deeply grateful to Dr. Lei Zuo, my advisor, for his unwavering guidance, invaluable insights, and continuous support throughout the course of this research. His expertise and mentorship have been instrumental in shaping this work. I extend my sincere appreciation to Dr. Hang Yu and Dr. Jiangtao Cheng, my committee members, for their valuable feedback, constructive criticism, and scholarly guidance that enriched this thesis. The financial support provided by the National Science Foundation (NSF) through Grant #2244686 was fundamental in advancing this research project. I am thankful for their investment and recognition of the importance of this endeavor. My heartfelt gratitude goes to my parents for their unending encouragement, unwavering belief in my capabilities, and for providing me with the opportunity to pursue cutting-edge research at Virginia Tech. Their support has been my anchor throughout this academic pursuit. I am also indebted to my friends, both here at Virginia Tech and back in India, whose unwavering moral support and companionship provided a sense of balance and kept me stress-free during these intense two years. Your presence has been a source of strength. Special thanks are due to my esteemed labmates, Dr. Gagan K Goyal and Haozheng Wang, whose insightful discussions and valuable inputs significantly enriched the course of my research. Their perspectives and collaborative spirit have been instrumental in shaping the ideas presented in this thesis. Lastly, I wish to express my heartfelt appreciation to all the individuals and participants who graciously dedicated their time, expertise, and insights to support this research endeavor. Their invaluable contributions were indispensable in shaping and enriching this work, playing a pivotal role in its realization.

Contents

List of Figures

List of Tables

List of Abbreviations

β_s	Solute expansion coefficient $[K^{-1}]$
β_T	Thermal expansion coefficient $[K^{-1}]$
Δt	Time step$[\tau_o]$
ΔX	Grid spacing$[W]$
$\dot{T}$	Cooling rate$[K/s]$
ϵ	Porosity
ϵ_4	Anisotropy strength
ϵ_b	Emissivity
Γ	Gibbs thomson coefficient$[mK]$
λ	Coupling constant
μ^+	Effective viscosity [kg $(ms)^{-1}$]
μ_s, μ_l	Solid and liquid viscosity [kg $(ms)^{-1}$]
ϕ	Phase field order parameter
ψ	Limiter function
ρ	Density [kg m^{-3}]
σ_b	Boltzmann constant $[Wm^{-2}K^{-4}]$

σ_s	Surface tension $[Nm^{-1}]$
τ_o	Relaxation time$[s]$
θ	Energy absorption coefficient
$\tilde{D}$	Dimensionless diffusion coefficient
$\tilde{l}_T$	Dimensionless thermal length
$\tilde{V}_P$	Dimensionless pulling velocity
$a_E, a_W, a_N, a_S, a_F, a_B, a_P$	TVD coefficients
c	Solute concentration$[wt\%Si]$
c_∞	Initial solute concentration$[wt\%Si]$
c_p	Specific heat $[J/K.kg]$
D	Liquid diffusion coefficient$[m^2s^{-1}]$
d_o	Thermal capillary length$[m]$
$F_e, F_w, F_n, F_s, F_f, F_b$	Convective mass flux$[kg/m^2s]$
f_s, f_l	Solid and liquid mass fraction
G	Temperature gradient$[K/m]$
g	Acceleration due to gravity $[ms^{-2}]$
H, h	Enthalpy $[J/kg]$
h_c	Convective heat transfer coefficient $[Wm^{-2}K^{-1}]$
k	Partition coefficient

k^+	Effective thermal conductivity $[W/mK]$
k_p, k_l, k_g	Solid, liquid, and gas thermal conductivity $[W/mK]$
L	Latent heat $[J/kg]$
l_T	Thermal length$[m]$
m	Liquidus line slope$[K(wt\%Si)^{-1}]$
q_o	Laser intensity $[Wm^{-2}]$
R	Laser diameter $[m]$
R	Solidification rate$[m/s]$
r	Ratio of gradients
S_h	Energy source term $[Wm^{-3}]$
S_u^{DC}	Deferred correction source term
T	Temperature $[K]$
t	Time $[s]$
T_a	Ambient temperature $[K]$
T_M	Material sintering temperature $[K]$
U	Dimensionless supersaturation
u, v, w	Velocities in x,y, and z directions [m s^{-1}]
U_b	Laser beam velocity [ms^{-1}]
V_P	Pulling velocity$[ms^{-1}]$

v_s, v_n	Velocity parallel and perpendicular to the surface $[ms^{-1}]$
W	Interfacial width$[m]$
AM	Additive Manufacturing
CFD	Computational Fluid Dynamics
DEM	Discrete Element Method
PDAS	Primary Dendritic Arm Spacing
SDAS	Secondary Dendritic Arm Spacing
SLM	Selective Laser Melting
TEG	Thermo Electric Generator
ZT	Thermoelectric Figure of Merit

Chapter 1

Introduction

1.0.1 Additive Manufacturing

Additive manufacturing, a cornerstone of modern manufacturing technologies, has seen substantial growth. According to the findings of Wohlers et al. [2], the anticipated trajectory indicates a continued expansion in the additive manufacturing (AM) industry in the coming years. Projections suggest that global sales within various industry sectors are poised to surpass the AU\$ 22.9 billion (US \$ 15.8 billion) mark. Additive manufacturing methods demonstrate versatility by facilitating the use of diverse materials, spanning metals, ceramics, and polymers. Notably, there's a growing focus and enthusiasm among researchers and industries toward metallic materials within the realm of AM. The American Society for Testing and Materials (ASTM) International Committee F42 categorizes additive manufacturing (AM) processes into seven distinct classifications[3], as outlined in Table 1.1. Powder bed fusion (PBF) processes constitute the primary methodology utilized in most metal additive manufacturing (AM) systems. Metal powder bed fusion (PBF) encompasses several prevalent techniques, including Electron Beam Melting (EBM), Direct Metal Laser Melting (DMLM), Selective Laser Melting (SLM), and Direct Metal Laser Sintering (DMLS) [3] among which SLM has seen significant advancements in the industry.

SLM[4], a powder bed fusion technology, involves the use of a high-power laser to selectively

Table 1.1: Types of AM

Sl No.	AM Category
1.	Directed Energy Deposition (DED)
2.	Powder Bed Fusion (PBF)
3.	Material Extrusion (ME)
4.	VAT Photopolymerization
5.	Material Jetting (MJ)
6.	Binder Jetting (BJ)
7.	Sheet Lamination (SL)

melt and fuse metallic powder particles layer by layer, building complex geometries from 3D digital models. After each layer is melted, the build platform is lowered, and a new layer of metal powder is spread over the previously solidified layer. The process repeats, layer by layer until the entire object is fabricated. As the layers bond, they form a solid, three-dimensional object with high precision and intricate geometries [5]. The schematic of SLM is depicted in Fig. 1.1.

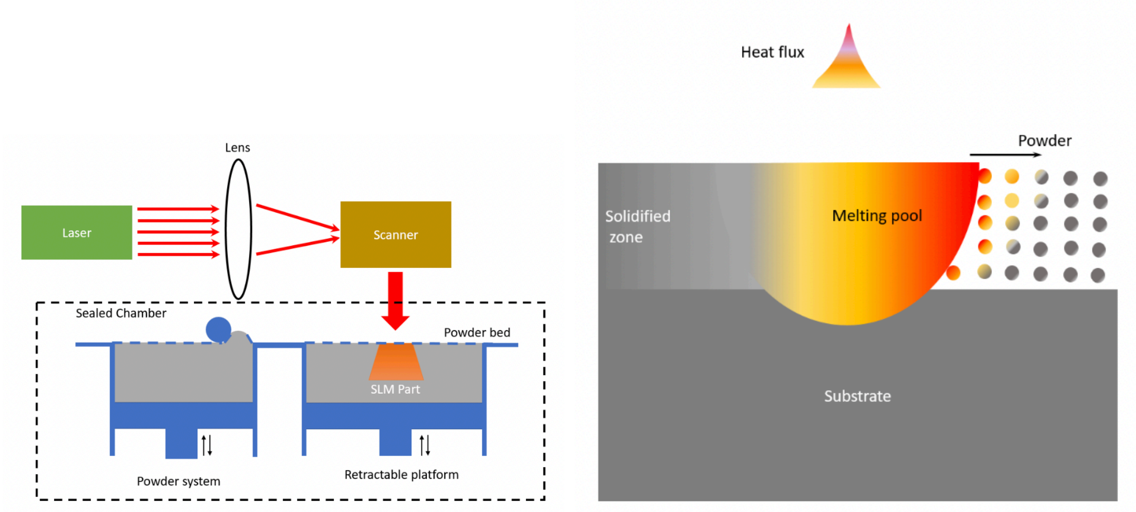

(a) SLM Setup

(b) SLM Physics

Figure 1.1: Schematic diagram of SLM

Because of its substantial energy density, SLM is well-suited for producing high-density parts using high melting point materials, eliminating the need for adhesives or binding agents in the fabrication process. This quality renders it highly advantageous for manufacturing thermoelectric materials, offering a suitable method for creating these materials with intricate designs and optimal density. This process is hence also ideal for applications in aerospace, medical implants, and automotive industries[6].

1.0.2 Thermoelectrics

Thermoelectric (TE) materials, known for their ability to convert heat into electricity and vice versa, have seen significant advancements through additive manufacturing techniques in recent years. Thimont and LeBlanc have [7] highlighted the possibility of creating thermoelectric generators (TEGs) featuring innovative leg designs, thanks to the advancements in additive manufacturing techniques. Mao et al. reported a zT of 0.8 at 400K with the $Bi_2Te_{2.7}Se_{0.3}$ deposited using SLM with a 100W laser. The effects of laser parameters on Se, Te vaporization, and balling within the printed material, secondary phases, and their effect on the transport properties have been discussed [8]. Yan et al. [9] introduced a non-equilibrium fabrication technique for n-type $CoSb_{2.85}Te_{0.15}$ utilizing Selective Laser Melting (SLM). They investigated the impact of processing parameters—specifically, laser power and scanning speed—on the deposited layer quality. Their analysis identified the optimal processing conditions within the SLM framework for this material. Zhang et al. [10] used single-step powder bed fusion, solidifying undoped Bi_2Te_3 powder with a continuous wave laser to obtain phase pure samples with a ZTmax of 0.11 at 50 °C using a 25 W laser. Shi et al. utilized a 30W laser to print porous $Bi_{0.5}Sb_{1.5}Te_3$ with a zTmax of 1.2 at 373K, with Bi, Sb, Te oxides as secondary phases [11]. Thus, there is finite success in utilizing the laser-based manufacturing methods for the established Bi_2Te_3 based thermoelectric materials. Mid-temperature (573-723K) application range TE materials such as Mg_2Si, Mg_3Sb_2 have seen significant progress in material development, metallization methods, and device prototyping using conventional methods [12, 13, 14, 15], although the application of laser manufacturing methods has not been tested yet. Zhang et al.[16] explored the thermal spraying of Mg_2Si and found that the rapid cooling led to point defects, ultimately boosting the ZT value. They drew parallels between SLM-based Additive Manufacturing (AM) and thermal spraying, highlighting shared traits like powder feeding, rapid cooling, and high automation. However, they emphasized SLM's notable advantages over thermal spraying, such as better process control for nanoparticle integration, higher mass density, milder fabrication conditions, decreased oxidation, and stronger bonding. Although, controlling the non-equilibrium synthesis conditions in SLM, especially with the presence of a high vapor pressure element Mg, is a challenge. Hence, a careful assessment of the processing conditions and their relation with the material properties is necessary to identify the suitable laser parameters. Qin et al. [17] and Li et al. [18] conducted studies on the growth patterns of Mg_2Si particles in Mg_2Si/Al composites. They concluded that the ultimate shape of the Mg_2Si crystals is influenced by both their inherent crystal structure and the conditions under which they grow. This finding is particularly important to consider in the context of SLM fabrication processes.

Magnesium silicide (Mg_2Si) is an inorganic compound notable for its face-centered cubic lattice structure. In its unit cell, it showcases an anti-fluorite arrangement. Specifically, Si^{4-} ions are located at both the corners and the face-centered positions, while Mg^{2+} ions occupy eight tetrahedral sites positioned within the structure's interior, illustrated in Fig. 1.2.

Despite Bi_2Te_3's high ZT, Mg_2Si's cost-effectiveness, abundance, and eco-friendly nature have established it as a widely used alternative in thermoelectric applications. While initially featuring a lower ZT, Mg_2Si's distinct advantages continue to drive its exploration and

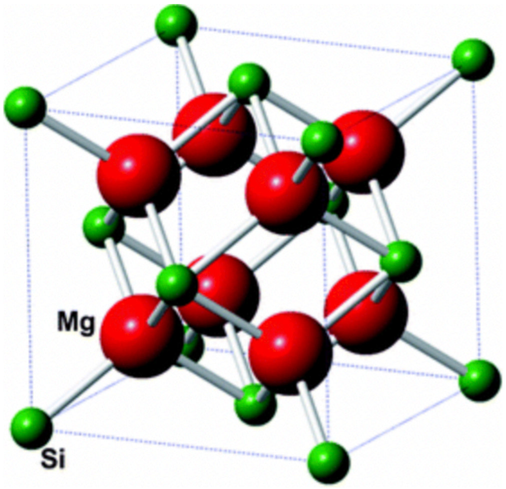

Figure 1.2: Mg_2Si Lattice Structure

development as a promising thermoelectric material. Farahi et al. [19] reported a ZT value of approximately 1.4 for Bi-doped Mg_2Si at 773 K, with an average ZT of 0.9 recorded between 400 and 773 K. These values were deemed considerably high for a wide range of thermoelectric applications.

1.0.3 Thermofluid Melt Pool Modeling

In the realm of additive manufacturing, specifically within Selective Laser Melting (SLM) processes applied to thermoelectric powders, understanding the thermo-fluid dynamics holds paramount importance. The temperature plays a crucial role in the SLM process. To understand the thermal changes in SLM, various three-dimensional heat transfer models have been developed by researchers[20, 21]. Addressing this concern involves leveraging two crucial tools: Computational Fluid Dynamics based heat and mass transfer modeling [22, 23], along with lattice Boltzmann simulations [24, 25]. The computational heat and mass transfer approach stands as a prevalent method utilized for modeling both the melting and resolidification processes. Ahmed et al.[20] conducted a 3D simulation study, detailed in [20], to analyze the distribution of temperature and stress within individual layers of 316L stainless steel formed atop a powder bed. This study utilized the commercial finite element software ANSYS for the analysis. In another model, Gu et al. Cai and Liang [21] developed an analytical thermal model which addresses variable scan strategies in selective laser melting (SLM) manufacturing, specifically considering angle discrepancies between layers. The model, utilized a transient moving point heat solution, accommodates multi-track and multi-layer effects, incorporating changes in thermal properties due to residual heat. Findings indicate that different scan directions minimally affected melt depth, while slight variations due to laser rotation angles show limited impact. However, scan strategies significantly alter thermal profiles and histories, laying groundwork for subsequent modeling of porosity and deflection in SLM manufacturing. [26] used the Discrete Element Method (DEM) and simulated the powder deposition in Selective Laser Melting for various materials, incorporating real particle size distributions. They investigated common SLM issues like the balling effect and layer fusion variations under different laser energies. The study resulted in optimized process parameters, such as energy density and hatch spacing, for improved continuity and efficiency in the SLM process for different powders. Whereas, the expanded model by Xiao and Zhang[22] analyzed a single-component metal powder bed in Selective Laser Melting, dividing the melting process into preheating, first melting, and second melting stages, and includes solutions accounting for shrinkage and gas volume fraction effects. Wu et al. [27] used a similar approach as done by Xiao and Zhang[22] to model the meltpool dynamics to manufacture Mg_2Si powders with SLM.

1.0.4 Microstructure Modeling

The layer-by-layer manufacturing approach inherent in the SLM process results in a complex thermal history. This complexity contributes to a microstructure characterized by porosity and anisotropy in the built part, which in turn can significantly impact the quality of the final product. Various numerical methods have been employed to simulate dendritic growth during the process of solidification. Cellular Automata[28] and phase field [29] methods are widely recognized as the most prevalent techniques for modeling dendrite growth during solidification in computational materials science. The phase field method stands out as a promising technique for dendrite growth modeling and is built on using continuous field variables to model the evolution of microstructures, like phase transitions and interface dynamics, in a diffuse interface framework. As outlined in the reference by Echebarria et al. [30], a refined phase-field model for directional solidification of binary alloys was introduced, overcoming solute trapping issues by incorporating an ”antitrapping” solute current. This addition allowed for better simulation of experimental scales, suppressing unwanted effects like surface diffusion and enabling precise modeling of interface kinetics even with mesoscopic parameters. Side branching plays a pivotal role in dendrite growth during directional solidification. A study by Echebarria et al. depicted a computational phase-field approach, revealing its origins—noise amplification and deterministic oscillations and its impacts on both two and three-dimensional settings. Notably, noise-induced sidebranching exhibited a smooth transition to nonlinear saturation. Surprisingly, increasing imposed thermal gradients unexpectedly reduced side branching onset velocity and wavelength due to tip blunting fostering noise amplification. These insights, vital in understanding sidebranching, are detailed in [31]. In another study by D.Tourret, and A. Karma depicting a two-dimensional phase-field study on columnar dendritic grain growth, the influence of temperature gradient and grain bicrystallography on the microstructure was examined ([32]). These findings challenge conventional assumptions, revealing that the elimination rate of misoriented grains and grain selection processes are complex and influenced by thermal fluctuations. These simulations align with experimental scaling laws but suggest that 3D grain bicrystallography significantly impacts grain selection by hindering sidebranching on misoriented grains.

Tian et al., as detailed in [29], employed a two-dimensional phase field model to simulate dendritic solidification within magnesium alloys. Their study unveiled significant insights into the effects of anisotropy and coupling coefficients on dendritic morphology. Enhanced computational efficiency was achieved through a parallel-adaptive mesh refinement algorithm, with findings aligning well with existing theoretical models. Furthermore, Wang et al., as outlined in [33], utilized the phase field method, guided by inputs from the CALPHAD database, to investigate the growth patterns of the Mg_2Si intermetallic layer within Mg-infiltrated Si-foams. Despite these advancements, challenges remain in the SLM process of thermoelectric Mg_2Si powders, particularly in controlling melt pool kinetics, including melting and solidification alongside fabrication. There remains a gap in the comprehensive numerical analysis of these dynamics for thermoelectric powders, which is crucial for process optimization.

This study aims to bridge this gap by presenting a detailed numerical analysis of melt pool kinetics in the SLM of thermo-electric powders, focusing on the melting and solidification process to refine the process parameters for the SLM fabrication of Mg_2Si. This paper is organized as follows. In chapter 2, we present the mathematical model used for developing the CFD-based melting dynamics and the phase field-based solidification dynamics. In section 3, we describe the numerical results, along with the optimized process parameters identified through the analysis. These optimized parameters were subsequently utilized for the actual fabrication of the Mg_2Si using SLM.

Chapter 2

Mathematical Model

2.0.1 Computational Fluid Dynamics Based Thermal Model

Physical Model

A Computational Fluid Dynamics model was developed to simulate the melt pool dynamics and obtain the temperature distribution during the fabrication of Mg_2Si using Selective Laser Melting. Fig. 2.1 depicts the manufacturing procedure utilized in the process. A Gaussian laser beam moving in the x direction at speed U_b is employed to melt the metal powders. Once the laser source moves away, the powder bed gradually cools and solidifies, culminating in the formation of a fully dense part. The computational domain's dimensions were set at 3.6 mm x 1.2 mm x 1.2 mm, a notably larger scale compared to the laser spot size and, consequently, the molten pool. Hence, the temperature fluctuation farther away from the molten pool was assumed to be very small. The molten pool was assumed to be symmetric, and hence, only half the molten pool was modeled to reduce the computational time.

Governing Equations

A one-phase model, as depicted in the reference Voller et al. [34], was used for the modeling. To account for the movement of the molten pool alongside the laser beam, the model adopts

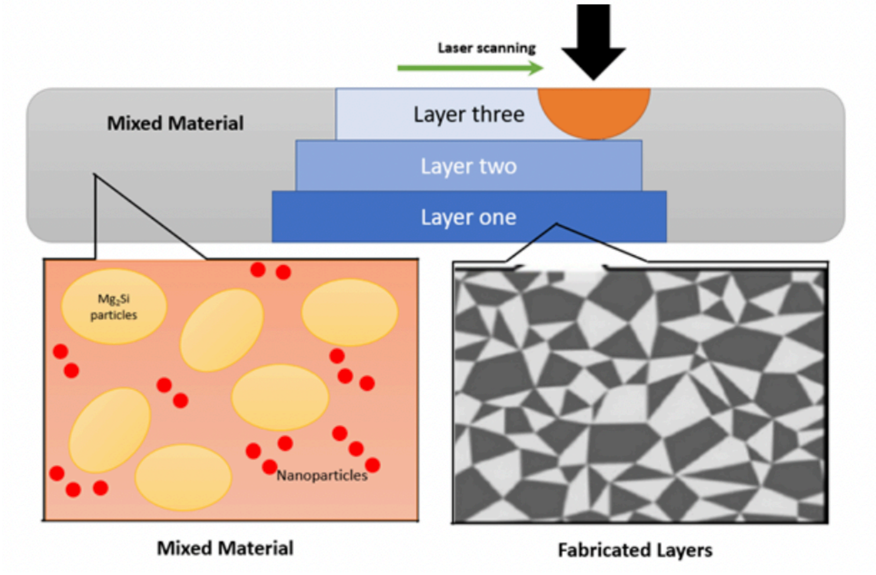

Figure 2.1: SLM Process

a moving reference frame, wherein the domain itself moves at a velocity denoted as U_b. A few assumptions were taken to simplify the problem:

1. The assumption made was that the powder bed's porosity remained consistent. As the melting phase progressed, the pressure from the liquid gradually displaced the gas present in the porous structure. Eventually, both the liquid and solidified areas expelled all remaining gas.

2. The Boussinesq approximation [35] was implemented in the Z direction to account for the buoyancy-driven flow and also reduce the computational expense.

3. The material has constant thermophysical properties, including the viscosity, specific heat, and thermal conductivity in each phase, and the variation in values during phase change is calculated with a weighted approach.

4. The model is developed for a single raster trajectory in the X-direction on the powder bed.

The governing equations were transformed into a unified single-phase model applicable to all regions within the computational domain. This was accomplished within a coordinate system that accounts for the domain's motion as follows:

- Continuity Equation

$$\frac{\partial \rho}{\partial t} + \frac{\partial(\rho(u-u_b))}{\partial x} + \frac{\partial(\rho v)}{\partial y} + \frac{\partial(\rho w)}{\partial z} \quad (2.1)$$

- X-Momentum Equation

$$\frac{\partial(\rho u)}{\partial t} + \frac{\partial(\rho u(u-u_b))}{\partial x} + \frac{\partial(\rho uv)}{\partial y} + \frac{\partial(\rho uw)}{\partial z} = -\frac{\partial P}{\partial x} + \frac{\partial}{\partial x}(\frac{\mu^+ \partial u}{\partial x}) + \frac{\partial}{\partial y}(\frac{\mu^+ \partial u}{\partial y}) + \frac{\partial}{\partial z}(\frac{\mu^+ \partial u}{\partial z}) \quad (2.2)$$

- Y-Momentum Equation

$$\frac{\partial(\rho v)}{\partial t} + \frac{\partial(\rho v(u-u_b))}{\partial x} + \frac{\partial(\rho vv)}{\partial y} + \frac{\partial(\rho vw)}{\partial z} = -\frac{\partial P}{\partial y} + \frac{\partial}{\partial x}(\frac{\mu^+ \partial v}{\partial x}) + \frac{\partial}{\partial y}(\frac{\mu^+ \partial v}{\partial y}) + \frac{\partial}{\partial z}(\frac{\mu^+ \partial v}{\partial z}) \quad (2.3)$$

- Z-Momentum Equation

$$\frac{\partial(\rho w)}{\partial t} + \frac{\partial(\rho w(u-u_b))}{\partial x} + \frac{\partial(\rho wv)}{\partial y} + \frac{\partial(\rho ww)}{\partial z} = -\frac{\partial P}{\partial z} + \frac{\partial}{\partial x}(\frac{\mu^+ \partial w}{\partial x}) + \frac{\partial}{\partial y}(\frac{\mu^+ \partial w}{\partial y}) + \frac{\partial}{\partial z}(\frac{\mu^+ \partial w}{\partial z}) + \rho g_r (T - T_e)(\beta_T + \beta_s C_s) \quad (2.4)$$

- Energy Equation

$$\frac{\partial(\rho h)}{\partial t}+\frac{\partial(\rho h(u-u_b))}{\partial x}+\frac{\partial(\rho hv)}{\partial y}+\frac{\partial(\rho hw)}{\partial z}$$
$$=\frac{\partial}{\partial x}(\frac{k^+\partial T}{\partial x})+\frac{\partial}{\partial y}(\frac{k^+\partial T}{\partial y})+\frac{\partial}{\partial z}(\frac{k^+\partial T}{\partial z})+S_h \quad (2.5)$$

The variables used in this context are: u, v, and w representing velocities along the X, Y, and Z axes correspondingly. P stands for pressure, denotes density, T signifies temperature, h represents enthalpy, k^+ denotes effective thermal conductivity, μ^+ stands for effective viscosity, β_T and β_s represent the thermal expansion coefficients for liquid and solute respectively, and C_s stands for the concentration of solute mass. The last term in Eq. 2.4 is the Boussinesq approximation term that accounts for the buoyancy in the molten pool, which is a volume effect. The source term S_h in Eq. 2.5 was used to model the enthalpy change during phase transition.

The powders were assumed to start melting at a temperature T_M - Δ T (Δ T = 200K) and completely melt at the melting temperature T_M. Hence, the mass fraction of liquid was defined separately in these temperature intervals as follows:

$$f_l=\begin{cases}1 & T\geq T_M\\ \frac{T_M-T}{\Delta T} & T_M-\Delta T<T<T_M\\ 0 & T\leq T_M-\Delta T\end{cases} \quad (2.6)$$

The fraction of solid powders in the mushy region is hence given by:

$$f_s=1-f_l \quad (2.7)$$

The effective thermal conductivity (k_{eff}) of the densely packed powder bed was computed utilizing the empirical correlation advocated by Hadley [36], a methodology further elaborated upon by Xiao et al. [22], outlined as follows:

$$\frac{k_{eff}}{k_g} = (1-\alpha_o)\frac{\epsilon f_o + (\frac{k_p}{k_g})(1-\epsilon f_o)}{1-\epsilon(1-f_o)+\epsilon(\frac{k_p}{k_g})(1-f_o)} + \alpha_o \frac{2(\frac{k_p}{k_g})^2(1-\epsilon)+(1+2\epsilon)(\frac{k_p}{k_g})}{(2+\epsilon)(\frac{k_p}{k_g})+1-\epsilon} \tag{2.8}$$

where

$$f_o = 0.8 + 0.1\epsilon, \tag{2.9}$$

$$\log \alpha_o = \begin{cases} -4.898\epsilon & 0 \leq \epsilon \leq 0.0827 \\ -0.405 - 3.154(\epsilon - 0.0827) & 0.0827 \leq \epsilon \leq 0.298 \\ -1.084 - 6.778(\epsilon - 0.298) & 0.298 \leq \epsilon \leq 0.580 \end{cases} \tag{2.10}$$

The effective thermal conductivity and viscosity within the melting mushy zone were determined by summing the properties of both the solid powders and the molten liquid, with each property weighted by its respective mass fraction, calculated as follows:

$$\mu^+ = \mu_s f_s + \mu_l f_l \tag{2.11}$$

$$k^+ = k_{eff} f_s + k_l f_l \tag{2.12}$$

The enthalpy of the powder was assumed to be temperature dependent and was calculated by:

$$h = \int_0^T c_{ps} dT \tag{2.13}$$

The enthalpy change during phase transition was dependent on the thermal capacity and the latent heat, which was given by:

$$\delta H = [\int_0^T (c_{pl} - c_{ps}) dT + L] f_l \tag{2.14}$$

As the thermal capacity of the sintered material stayed consistent throughout fabrication, the simplification extended to the enthalpy change as follows:

$$\delta H = \begin{cases} L & T \geq T_M \\ L f_l & T_M - \Delta T < T < T_M \\ 0 & T \leq T_M - \Delta T \end{cases} \tag{2.15}$$

Finally, the source term S_h in the energy equation consisted of transient and convective terms and was calculated as taken in ref. [34] as follows:

$$S_h = -\frac{\partial}{\partial t}(\rho \delta H) - \frac{\partial}{\partial x}(\rho (u - u_b) \delta H) - \frac{\partial}{\partial y}(\rho v \delta H) - \frac{\partial}{\partial z}(\rho w \delta H) \tag{2.16}$$

Boundary Conditions

Boundary conditions are defined on each face of the given computational domain as follows:

- **Boundary A**(Top face of the domain in Fig. 2.2): A heat transfer balance was conducted along this boundary to establish the temperature boundary condition. Within this setup, a portion of the heat absorbed by the powder bed from the Gaussian laser beam dissipated into the environment through convection and radiation. Concurrently, another portion of the heat transferred through conduction into the powder bed. The specific values for the convective heat transfer coefficient and emissivity were referenced from literature sources [37, 38]. The implementation of this condition occurred as follows:

$$-k_{eff}\frac{\partial T}{\partial z}_{z=s} = \theta q_{laser} + h_c(T - T_a) + \epsilon_b \sigma_b (T^4 - {T_a}^4) \tag{2.17}$$

where,

$$\theta = \begin{cases} 1 & Laser spot \\ 0 & Rest of the area \end{cases} \tag{2.18}$$

The heat flux of the Gaussian laser beam is given as follows:

$$q_{laser} = -\frac{q_o}{\pi R^2} \exp\left\{(-\frac{r^2}{R^2})\right\} \tag{2.19}$$

The shear force and surface tension were assumed to be balanced at the top surface for the velocity boundary condition as follows:

$$\mu^+(\frac{\partial v_s}{\partial n} + \frac{\partial v_n}{\partial s}) = \frac{\partial \sigma}{\partial T}\frac{\partial T}{\partial s} \tag{2.20}$$

The variables v_s and v_n represent the tangential and normal components of velocity at the heating surface, respectively.

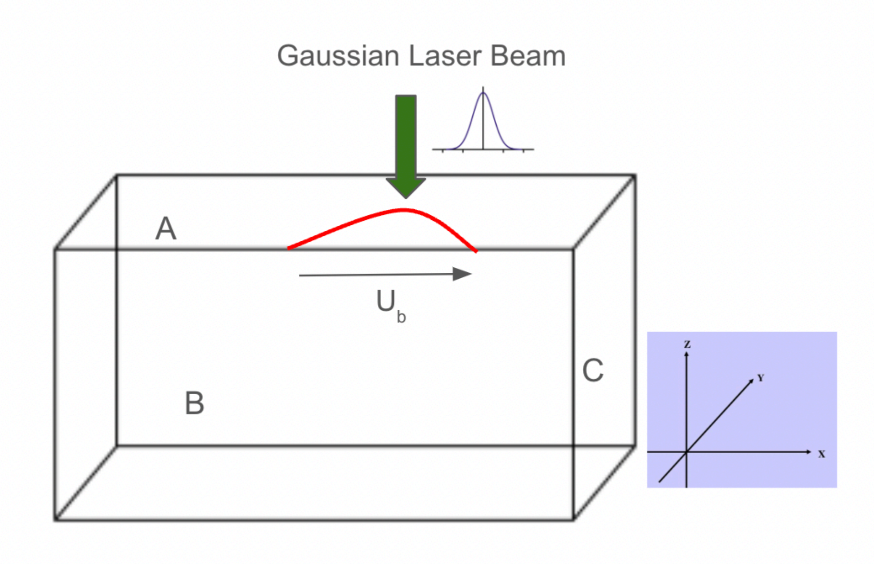

Figure 2.2: Computational Domain

- **Boundary B**(Front face of the domain in Fig. 2.2): This face is symmetrical, and hence symmetry boundary conditions are applied here as follows:

$$\frac{\partial T}{\partial y}_{y=0} = 0 \tag{2.21}$$

$$\frac{\partial u}{\partial y}_{y=0} = \frac{\partial w}{\partial y}_{y=0} = v_{y=0} = 0 \tag{2.22}$$

- **Boundary C**(Right, left, and bottom faces of the domain in Fig. 2.2): Given the considerable size of the computational domain and the relatively low thermal conductivity of the material, the right, left, and bottom boundaries were significantly distant from the laser spot. Consequently, these faces were assumed to maintain a constant temperature equivalent to the ambient temperature:

$$T = T_a \tag{2.23}$$

The velocities on these boundaries were assumed to be zero as there was no particle motion away from the melt pool.

$$u = v = w = 0 \tag{2.24}$$

Numerical Procedures

The simulated case is a quasi-steady state, three-dimensional, non-linear problem. A false transient method is used to solve the problem, and a steady state is said to be obtained when the temperature and velocity distribution do not change with time. A Finite Volume-based approach was employed by dividing the domain into multiple control volumes and solving the governing equations in each control volume. The SIMPLER algorithm, introduced by Patankar [39], was employed to solve the governing equations 2.1-2.5. The equations were discretized using the Total Variation Diminishing (TVD) Scheme proposed by Van Leer [40] as it's second-order accurate and unconditionally stable without overshoot as used in reference [27]. The flux limiter function used in this scheme is given by:

$$\psi(r) = \frac{r + |r|}{1 + r^2} \tag{2.25}$$

The above limiter function is chosen so that the denominator is never zero, hence making the simulation stable.

The discretization for the 3D cartesian grid system was adapted from the 2D scheme described in Versteeg and Malalasekera's book [41] as given below:

$$\begin{aligned} a_P\phi_P = {} & a_W\phi_W + a_E\phi_E + a_S\phi_S \\ & + a_N\phi_N + a_F\phi_F + a_B\phi_B + {S_u}^{DC} + S_\phi \end{aligned} \tag{2.26}$$

Where the superscripts W, E, S, N, F, and B are the West, East, South, North, Front, and Back faces of the control volume, respectively, as shown in Fig. 2.3.

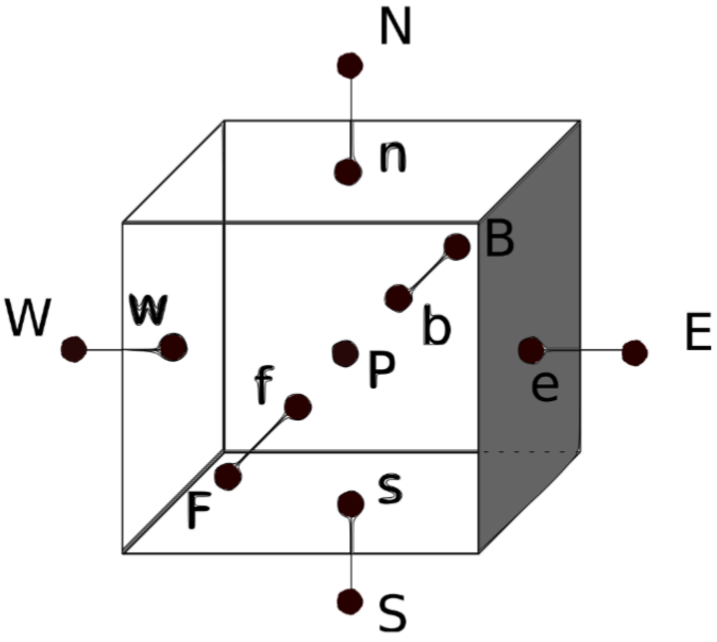

Figure 2.3: A single control volume

The coefficient a_P is given by:

$$a_P = a_E + a_W + a_N + a_S + a_B + a_F + (F_e - F_w) + (F_n - F_s) + (F_b - F_f) \quad (2.27)$$

where the deferred correction source term ${S_u}^{DC}$ is given by:

$$
\begin{aligned}
{S_u}^{DC} = \frac{1}{2}F_e[(1-\alpha_e)\psi({r_e}^-) - \alpha_e\psi({r_e}^+)](\phi_E - \phi_P) \\
+ \frac{1}{2}F_w[-(1-\alpha_w)\psi({r_w}^-) + \alpha_w\psi({r_w}^+)](\phi_P - \phi_W) \\
+ \frac{1}{2}F_n[(1-\alpha_n)\psi({r_n}^-) - \alpha_n\psi({r_n}^+)](\phi_N - \phi_P) \\
+ \frac{1}{2}F_s[-(1-\alpha_s)\psi({r_s}^-) + \alpha_s\psi({r_s}^+)](\phi_P - \phi_S) \\
+ \frac{1}{2}F_b[(1-\alpha_b)\psi({r_b}^-) - \alpha_b\psi({r_b}^+)](\phi_B - \phi_P) \\
+ \frac{1}{2}F_f[-(1-\alpha_f)\psi({r_f}^-) + \alpha_f\psi({r_f}^+)](\phi_P - \phi_F)
\end{aligned}
\tag{2.28}
$$

where ${r_e}^+$, ${r_e}^-$, ${r_w}^+$, ${r_w}^-$, ${r_n}^+$, ${r_n}^-$, ${r_s}^+$, ${r_s}^-$, ${r_b}^+$, ${r_b}^-$, ${r_f}^+$, and ${r_f}^-$ are defined as given in [41].

For modeling purposes, uniformly structured hexahedral grids measuring 150 units in the X direction, 75 units in the Y direction, and 75 units in the Z direction were employed. To ensure numerical stability in line with the CFL condition, a false time step of 0.0001 seconds was selected. The inner iterative process persisted until the residuals of all governing equations reached a threshold below 10^{-5}. Convergence of the solution was determined when $|\frac{\phi_N - \phi_{N-1}}{\phi_N}| < 10^{-3}$. To solve the equations, the Alternating Direction Implicit solver was utilized, and to expedite convergence, the Block Correction Method described in [27] was employed. The entire code was developed using MATLAB.

Material Properties

The thermal conductivity values of Mg_2Si in the solid and liquid phase were defined according to the measured values of Mg_2Si thermal conductivity in a wide temperature range

[42, 43, 44]. It is to be noted that the thermal conductivity values of these powders decrease with the increase in temperature, and hence, the liquid and solid thermal conductivities were approximated accordingly after sufficient testing. The sintering temperature of Mg_2Si is known to be in the range of 850°C - 900°C from the reference [45] and is set at (1173K)900°C for this study. It is also worth noting that the melting point of bulk Mg_2Si is known to be 1375K [46]. Hence, a few initial tests were run by setting the sintering temperature to 1375K and were tested experimentally, as discussed in the results. The comprehensive set of material properties and input parameters employed for the ultimate simulation can be found in the data presented within Table 2.1.

Table 2.1: Simulation Parameters - CFD

Input	Value	Unit
Specific heat (c_p)	67.87[46]	$Jkg^{-1}K^{-1}$
Solid thermal conductivity (k_p)	5[42, 43, 44]	$Wm^{-1}K^{-1}$
Liquid thermal conductivity (k_l)	3.5[42, 43, 44]	$Wm^{-1}K^{-1}$
Gas thermal conductivity (k_g)	0.024[36]	$Wm^{-1}K^{-1}$
Porosity (ϵ)	0.2	
Density (ρ)	1990[46]	kgm^{-3}
Liquid viscosity (μ_l)	5×10^{-3}[46]	$kgm^{-1}s^{-1}$
Solid viscosity (μ_s)	1×10^{4}[22]	$kgm^{-1}s^{-1}$
Latent heat (L)	4.5×10^{5}[46]	Jkg^{-1}
Sintering temperature (T_M)	900[45]	°C
Thermal expansion coeff. (β_T)	1.1×10^{-5}[46]	K^{-1}
Ambient temperature (T_a)	298.15	K
Convective heat transfer coeff.(h_c)	10[22]	$Wm^{-2}K^{-1}$
Laser diameter (R)	0.2	mm
Laser power (Q)	10-15	W
Scanning speed (u_b)	0.05-0.2	ms^{-1}
Boltzmann constant (σ_b)	5.67×10^{-8}	$Wm^{-2}K^{-4}$
$\partial\sigma/\partial T$	-10^{-5}[22]	$kgs^{-2}K$
Radiation emissivity (ϵ_b)	0.86[27]	

2.0.2 Phase Field Model

Governing Equations

This study employed a phase field-based approach to simulate the microstructure growth of Mg_2Si in Selective Laser Melting (SLM). The phase field order parameter, a key component in the simulation, dynamically evolves based on the governing equations of the phase field, which are intricately coupled with the heat and solute diffusion equations. The simulation methodology followed a directional solidification of dilute binary alloys approach, introducing a smooth yet rapid variation in the order parameter value at the interface developed by Echebarria et al. [30]. Within the model, a significant addition was the incorporation of a corrective anti-trapping current. This was purposefully introduced to offset the undesired solute trapping, a phenomenon linked to the sudden change in chemical potential at the interface [47]. Several assumptions were taken into account while formulating the phase field model [48].

1. The model assumes that convection within the liquid has a negligible impact, attributing the mass transport entirely to diffusion mechanisms.

2. The influence of latent heat of fusion is disregarded by imposing the temperature field in the form of a gradient.

3. Constant thermophysical properties are assumed throughout the simulation without accounting for variations.

4. Due to the substantial difference in magnitudes, with the solute diffusivity in the solid being two orders of magnitude lower than in the liquid, the solute diffusivity in the solid state is omitted from consideration.

5. The model assumes local equilibrium at the solid-liquid interface.

The model's constitutive equations were specifically selected as Eq.(68) and Eq.(69) outlined in reference [30]. Utilizing the phase field variables from [49], the governing equations in dimensionless form for the phase field order parameter and the concentration variable in two dimensions are expressed as follows:

$$\begin{aligned}\left[1-(1-k)\frac{x-\tilde{V}_P t}{\tilde{l}_T}\right](a_s(\theta))^2\frac{\partial\phi}{\partial t} &= \boldsymbol{\nabla}\cdot\big((a_s(\theta))^2\boldsymbol{\nabla}\cdot\phi\big)\\ &\quad+\sum_{m=x,y}\left[\partial_m(|\boldsymbol{\nabla}\cdot\phi|^2)a_s(\theta)\frac{\partial a_s(\theta)}{\partial(\partial_m\phi)}\right]\\ &\quad+\phi-\phi^3-\lambda(1-\phi^2)^2\left(U+\frac{x-\tilde{V}_P t}{\tilde{l}_T}\right)\end{aligned} \tag{2.29}$$

$$\begin{aligned}\left(\frac{1+k}{2}-\frac{1-k}{2}\phi\right)\frac{\partial U}{\partial t} &= \boldsymbol{\nabla}\cdot\left(\tilde{D}\frac{1-\phi}{2}\boldsymbol{\nabla}\cdot U\right)\\ &\quad+\boldsymbol{\nabla}\cdot\left(\frac{1}{2\sqrt{2}}\left[1+(1-k)U\right]\frac{\partial\phi}{\partial t}\frac{\boldsymbol{\nabla}\cdot\phi}{|\boldsymbol{\nabla}\cdot\phi|}\right)\\ &\quad+\big(1+(1-k)U\big)\frac{1}{2}\frac{\partial\phi}{\partial t}\end{aligned} \tag{2.30}$$

with

$$U=\frac{1}{1-k}\left[\frac{\frac{c}{{c_l}^o}}{\frac{(1-\phi)}{2}+k\frac{(1+\phi)}{2}}-1\right] \tag{2.31}$$

In this context, ϕ represents the phase field order parameter, where ϕ equals 1 in the solid phase and ϕ equals -1 in the liquid phase. U stands for the generalized dimensionless supersaturation, while c denotes the solute concentration field. ${c_l}^o$ is defined as $\frac{c_\infty}{k}$, representing the solute concentration of a flat interface at a reference (Solidus) temperature T_o for an alloy with a solute concentration of c_∞ and a solute partition coefficient k as detailed in [32].

Space is scaled in units of the interfacial width W, and time is scaled in units of the relaxation time τ_o according to [30]. The non-dimensionalized values of the diffusion coefficient $\tilde{D}$, pulling velocity $\tilde{V}_P$, and thermal length $\tilde{l}_T$ are given as follows:

$$\tilde{D} = \frac{D\tau_o}{W^2} = a_1 a_2 \frac{W}{d_o} \tag{2.32}$$

$$\tilde{V}_P = \frac{V_P \tau_o}{W} = a_1 a_2 \frac{V_P d_o}{D} \left(\frac{W}{d_o}\right)^2 \tag{2.33}$$

$$\tilde{l}_T = \frac{l_T}{W} = \frac{l_T}{d_o} \frac{1}{(\frac{W}{d_o})} \tag{2.34}$$

and the coupling constant λ is as follows:

$$\lambda = a_1 \frac{W}{d_o} \tag{2.35}$$

The value of λ should be sufficiently small to ensure the convergence of the simulation while avoiding unnecessary computational expenses [50]. The thermal length l_T is given by:

$$l_T = \frac{|m| c_\infty (\frac{1}{k} - 1)}{G} \tag{2.36}$$

where G is the temperature gradient input into the computational domain, m is the slope of the liquidus line, and the capillary length d_o is given by:

$$d_o = \frac{\Gamma}{\left[|m|c_\infty(\frac{1}{k} - 1)\right]} \tag{2.37}$$

with Γ the Gibbs Thomson coefficient of the solid-liquid interface, where $a_1 = 0.8839$, and $a_2 = 0.6267$. The relaxation time τ_o is:

$$\tau_o = \frac{a_2 \lambda W^2}{D} \tag{2.38}$$

The surface tension anisotropy is taken to be a four-fold anisotropy as taken in the reference [32, 48] and is given by:

$$a_s(\theta) = 1 + \epsilon_4 \cos(4\theta) \tag{2.39}$$

In this scenario, ϵ_4 represents the strength of anisotropy, while θ denotes the angle between the normal to the interface and a set crystalline axis. The anisotropy is discretized by expressing θ in terms of ϕ as depicted below:

$$\theta = \tan^{-1}\left(\frac{\partial_y \phi}{\partial_x \phi}\right) \tag{2.40}$$

The detailed discretization and development of Eq. (29) and Eq. (30) are taken from Appendices B and C in ref. [32].

Implementation

The phase field Eq. (2.29), and Eq. (2.30), are discretized and solved using the Finite Difference Method on a grid of square elements with spacing ΔX. The Euler explicit scheme is used to march ahead in time with a time step Δt. The first and second terms on the right-hand side of Eq.(2.29) involving anisotropy are solved by converting them into first and second-order spatial derivatives of ϕ. The first term on the RHS of Eq. 2.29, can be expanded using the chain rule as depicted below:

$$\boldsymbol{\nabla} \cdot \big((a_s(\theta))^2 \boldsymbol{\nabla} \cdot \phi\big) = \boldsymbol{\nabla} \cdot \big((a_s(\theta))^2\big) \boldsymbol{\nabla} \cdot \phi + \big((a_s(\theta))^2\big) \nabla^2 \phi \tag{2.41}$$

where

$$\boldsymbol{\nabla} \cdot \big((a_s(\theta))^2\big) \boldsymbol{\nabla} \cdot \phi = \big(\partial_x \phi \partial_x \theta + \partial_y \phi \partial_y \theta) 2 {a_s}' a_s [32] \tag{2.42}$$

and, for the Laplacian of the phase field, a standard five-point stencil is used with a maximally isotropic discretization as mentioned in Appendix B of the reference [30] as follows:

$$\begin{aligned} \nabla^2(\phi_{i,j}) = \frac{2}{3}\Big[&\big(\phi_{i-1,j} + \phi_{i+1,j} + \phi_{i,j-1} + \phi_{i,j+1}\big) \\ &+ \frac{1}{4}\big(\phi_{i-1,j+1} + \phi_{i+1,j+1} + \phi_{i-1,j-1} + \phi_{i+1,j-1}\big) - 5\phi_{i,j}\Big] \Big/ (\Delta X)^2 \end{aligned} \tag{2.43}$$

The second term on the RHS of Eq. 2.29 can be expanded as depicted in ref. [32] as follows:

$$\sum_{m=x,y} \left[\partial_m (|\boldsymbol{\nabla} \cdot \phi|^2) a_s(\theta) \frac{\partial a_s(\theta)}{\partial(\partial_m \phi)}\right] = \big(\partial_x \phi \partial_y \theta + \partial_y \phi \partial_x \theta\big) \big[{a_s}'' a_s + {a_s}'^2\big] \tag{2.44}$$

where

$$a_s = a_s(\theta) = 1 + \epsilon_4 \cos 4\theta \tag{2.45}$$

$$a_s = a_s'(\theta) = -4\epsilon_4 \sin 4\theta \tag{2.46}$$

$$a_s = a_s''(\theta) = -16\epsilon_4 \cos 4\theta \tag{2.47}$$

Since $\cos\theta = \frac{\partial_x \phi}{|\boldsymbol{\nabla} \cdot \phi|}$, and $\sin\theta = \frac{\partial_y \phi}{|\boldsymbol{\nabla} \cdot \phi|}$, the expressions for $\cos 4\theta$ and $\sin 4\theta$ can be calculated as follows:

$$\cos(4\theta) = 1 - 2\sin^2(2\theta) = 1 - 8\cos^2\theta \sin^2\theta = 1 - 8\frac{(\partial_x\phi)^2(\partial_y\phi)^2}{|\nabla\phi|^4} \tag{2.48}$$

$$\begin{aligned} \sin(4\theta) = 2\sin(2\theta)\cos(2\theta) = 4\sin\theta\cos\theta(\cos^2\theta - \sin^2\theta) \\ = 4\Big[\frac{(\partial_x\phi)^3\partial_y\phi - \partial_x\phi(\partial_y\phi)^3}{|\nabla\phi|^4}\Big] \end{aligned} \tag{2.49}$$

The detailed calculations were done as depicted in Appendix B of the reference [32]. The first and second terms on the right-hand side of Eq. (2.30) are the terms accounting for the liquid diffusion and the anti-trapping current (developed by Echebarria et al. [30]), respectively, which are the terms involving the divergence are developed as per the formulation given in the reference [32]. The anti-trapping current serves to enable a solute flow perpendicular to the diffuse interface, moving from the solid to the liquid. This action helps offset the inclination of phase-field models to exhibit unrealistically high levels of solute trapping.

These values at a point (i,j) are calculated by taking an aggregate of their contributions at every link across the given node. For instance, $[\vec{v}]_{i+\frac{1}{2},j}$, is the contribution of a field $[\vec{v}]$ on the link between the nodes (i,j) and (i+1,j) as depicted in Fig. 2.4. Hence, the discretization of the divergence of $[\vec{v}]$ at node (i,j) is established as follows:

$$[\vec{v}]_{i,j} = \frac{1}{\Delta X}\left([\vec{v}]_{i-\frac{1}{2},j} + [\vec{v}]_{i+\frac{1}{2},j} + [\vec{v}]_{i,j-\frac{1}{2}} + [\vec{v}]_{i,j+\frac{1}{2}}\right) \tag{2.50}$$

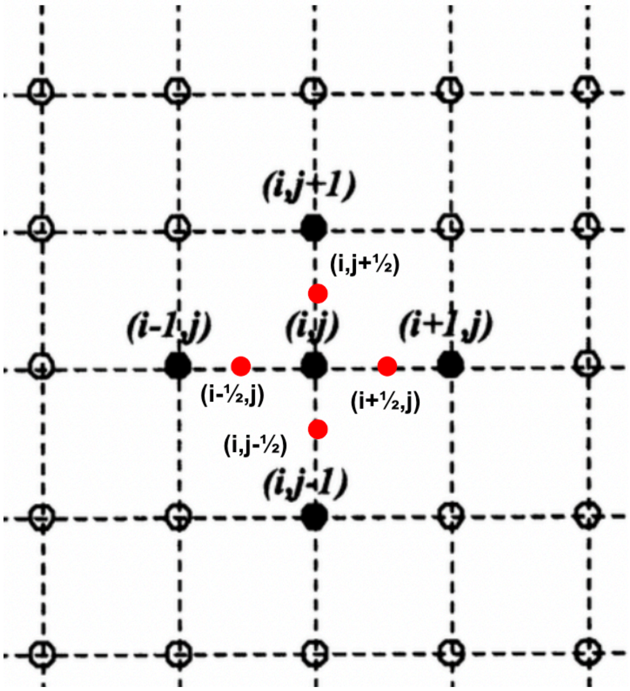

Figure 2.4: Finite Difference Grid

As per ref.[32], the first term on the RHS of Eq. (2.30) (diffusion term) is calculated by taking the average on the link. For instance, at (i+1/2,j):

$$[(1-\phi)\nabla U]_{i+\frac{1}{2},j} = \left[\frac{2-\phi_{i,j}-\phi_{i+1,j}}{2}\right]\left[\frac{U_{i+1,j}-U_{i,j}}{\Delta X}\right] \tag{2.51}$$

The calculation of the second term on the right-hand side of Equation (2.30) (referred to as the antitrapping term) involves averaging $\left[1+(1-k)U\right]\frac{\partial\phi}{\partial t}/2$ and then multiplying it by the interface normal $\left(\frac{\boldsymbol{\nabla}\cdot\phi}{|\boldsymbol{\nabla}\cdot\phi|}\right)$. This process accounts for the direction of the anti-trapping current. Consequently, the contribution of the anti-trapping current on the $(i+\frac{1}{2},j)$ link is detailed in [32].

$$\left[\frac{1}{2\sqrt{2}}\big[1+(1-k)U\big]\frac{\partial\phi}{\partial t}\frac{\boldsymbol{\nabla}\cdot\phi}{|\boldsymbol{\nabla}\cdot\phi|}\right]_{i+\frac{1}{2},j}=\frac{1}{2}\left[\frac{1}{2\sqrt{2}}\big[1+(1-k)U_{i,j}\big]\frac{\partial\phi_{i,j}}{\partial t}\right.$$
$$\left.+\frac{1}{2\sqrt{2}}\big[1+(1-k)U_{i+1,j}\big]\frac{\partial\phi_{i+1,j}}{\partial t}\right]\times\frac{\big[\partial_x\phi\big]_{i+\frac{1}{2},j}}{\left\{\left(\big[\partial_x\phi\big]_{i+\frac{1}{2},j}\right)^2+\left(\big[\partial_y\phi\big]_{i+\frac{1}{2},j}\right)^2\right\}^{\frac{1}{2}}}\qquad(2.52)$$

The element of $\nabla\phi$ that aligns with the direction of the specific link at $(i+\frac{1}{2},j)$ is given by:

$$\big[\partial_x\phi\big]_{i+\frac{1}{2},j}=\frac{\phi_{i+1,j}-\phi_{i,j}}{\Delta X}\qquad(2.53)$$

The element perpendicular to the specified link is computed by averaging the central difference at both ends of the link, resulting in the value at $(i+\frac{1}{2},j)$:

$$\big[\partial_y\phi\big]_{i+\frac{1}{2},j}=\frac{1}{2}\left(\frac{\phi_{i,j+1}-\phi_{i,j-1}}{2\Delta X}+\frac{\phi_{i+1,j+1}-\phi_{i+1,j-1}}{2\Delta X}\right)=\frac{\phi_{i,j+1}-\phi_{i,j-1}+\phi_{i+1,j+1}-\phi_{i+1,j-1}}{4\Delta X}\qquad(2.54)$$

The computations within the bulk phase involve calculating the anisotropy terms (those with an ϵ_4 factor in Eq. (2.29)) and the anti-trapping current solely when $\nabla^2\phi\geq 10^{-6}$. These effects are specific to the vicinity of the solid-liquid interface and are set to zero otherwise. Furthermore, the first term on the right-hand side of Eq. (2.30), representing the solute diffusion term, is computed only when $(1-\phi)\geq 10^{-6}$ according to reference [32]. This condition arises as solid-state diffusion is considered negligible and thus nullified within the bulk solid phase.

A solid seed of radius r is defined at the bottom of the 2D computational domain, and the initial solute concentration field c in the solid and liquid phase is defined as kc_∞ and c_∞, respectively, when the solidification starts as taken in reference [30]. No flux boundary condition is set on all four sides of the 2D computational domain.

In order to disrupt the initial planar interface and induce the emergence of side branches at each grid point (i, j) during each time step, a random perturbation $\eta\beta_{i,j}\sqrt{\Delta t}$ [32] is incorporated into the value of $\phi_{i,j}$ at the subsequent time step as follows:

$$\phi_{i,j}(t + \Delta t) = \phi_{i,j}(t) + \Delta t\frac{\partial \phi_{i,j}}{\partial t} + (1 - \phi^2)\eta\beta_{i,j}\sqrt{\Delta t} \tag{2.55}$$

The value $\beta_{i,j}$ represents a random number uniformly distributed within the range [-0.5, 0.5], while η denotes the noise amplitude, set specifically at 0.01 [32]. Δt signifies the time step used in calculations. The inclusion of the prefactor $(1 - \phi^2)$ alongside the perturbation helps confine the noise to the region near the interface where $\phi \neq \pm 1$. The entire programming process was conducted using MATLAB.

Simulation Parameters

The parameters used for the simulation are depicted in Table 2.2. The value of λ is selected to be 35, which is the smallest tested value that assures the convergence of the simulation. Using this, the value of W and τ_o were calculated with the respective equations mentioned in the governing equations section above. The value of ΔX is taken to be 0.8 times the interfacial width W as taken in reference [30] to assure the capture of the interfacial phenomenon. The time step is set at $0.007\tau_o$ to assure the numerical stability for the diffusion equation in 2 dimensions for the Euler explicit scheme, which is given by the condition:

$$\Delta t < \frac{(\Delta X)^2}{4D} \tag{2.56}$$

The slope of the liquidus line for 10 wt% Si is calculated from the phase diagram for Mg-Si alloys as depicted in Fig. 2.5. The blue line indicates the wight percent of Si used for the calculation and the red line is a tangent drawn at the intersection of the blue line with the liquidus line in the phase diagram. The slope of this red line is calculated using WebPlotDigigitizer and is depicted in Table 2.2.

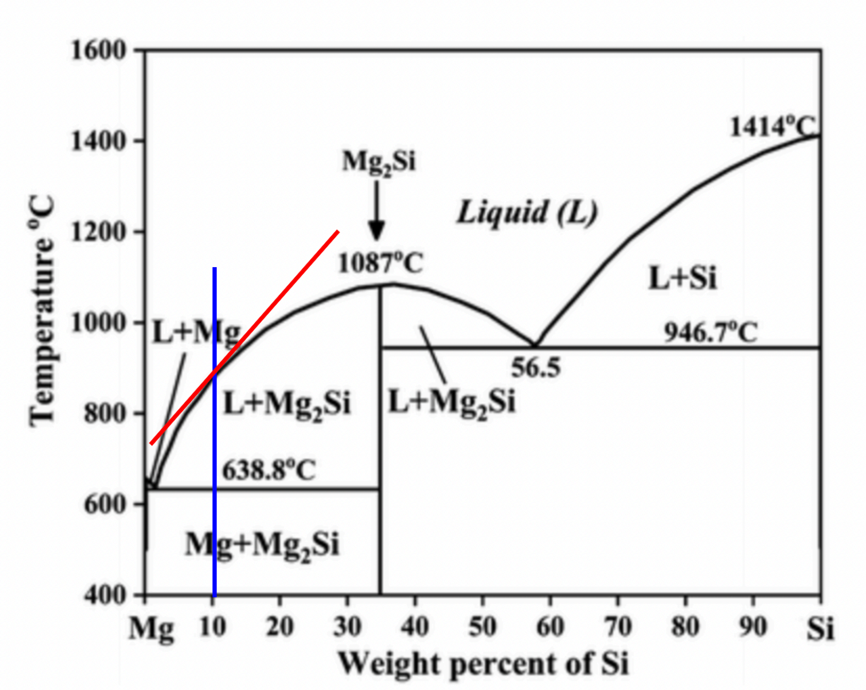

Figure 2.5: Slope calculation from the phase diagram

Table 2.2: Simulation Parameters - Phase Field

Input	Value	Unit
Domain	10×10	μm^2
Mesh	1118×1118	
Initial solute concentration (c_∞)	10	wt% Si
Partition coefficient (k)	0.3	
Liquid diffusion coefficient (D)	9×10^{-9}[51]	$m^2 s^{-1}$
Liquidus line slope (m)	15.83	K $(wt\%Si)^{-1}$
Gibbs Thomson coefficient (Γ)	7.46×10^{-8}[52]	mK
Anisotropy strength (ϵ_4)	0.002	
Thermal capillary length (d_o)	2.022×10^{-10}	m
Interfacial Width (W)	1.12×10^{-8}	m
Coupling constant (λ)	35	
Relaxation time (τ_o)	3.05×10^{-7}	s
Pulling Velocity (V_P)	0.05-0.1	ms^{-1}
Seed Diameter (r)	0.35	μm
Grid spacing (ΔX)	0.8	W
Time step (Δt)	0.007	τ_o

Chapter 3

Results And Discussion

3.0.1 Computational Fluid Dynamics Results

Code Validation

The developed code underwent validation by simulating the laser melting process on a non-porous 6063 aluminum sheet. The dimensions of the sheet was set as 229 x 152 x 3.2mm to match the experimental study by Kou and Wang [53]. In their experiments, a continuous wave CO2 laser with a power of 1.3KW and a scanning speed of 4.23 mm/sec was utilized. Kou and Wang observed an 86% heat loss from the surface area due to convection, conduction, and radiation, measuring the power absorbed calorimetrically. The simulation employed the same physical properties as those documented in the literature for porous aluminum sheets [53].

The comparison of the melt pool fusion boundaries between the in-house developed model and the simulated[22]/experimental values from the literature is illustrated in Fig. 3.1. The fusion boundaries displayed a close alignment with standard results, exhibiting minor variations primarily at the edges of the molten pool. This slight variance can be attributed to differences in the Gaussian laser profile considered in this work compared to the actual laser energy distribution. Hence, this comprehensive comparison demonstrates the validity of the developed code in simulating the laser melting process.

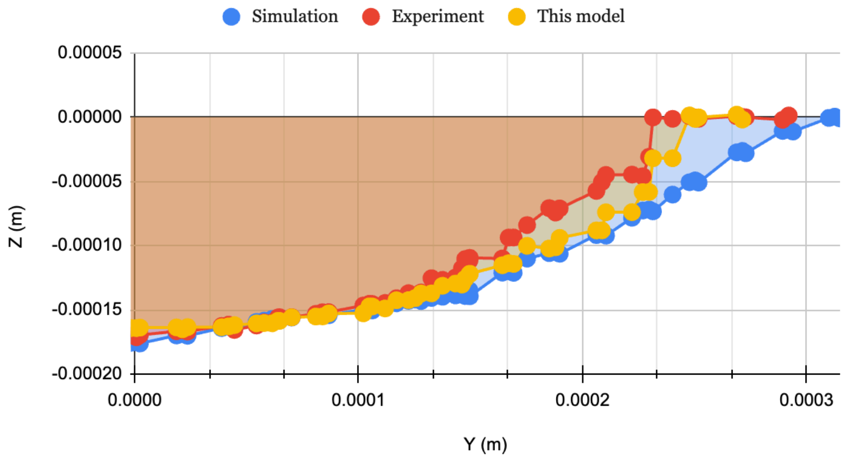

Figure 3.1: Fusion boundary comparison with standard results

First run - Thermally Favourable Process Parameters

As discussed in Section 2.1.5, a few sets of initial tests were run by setting the melting point of Mg_2Si to 1375K at a higher solid and liquid thermal conductivity value with a bigger spot size. The parameters used for this run that are different from the ones mentioned in Table 2.1 are depicted in Table 3.1. Laser powers of 20W - 40W were tested with scanning speeds ranging from 0.04 ms^{-1} to 0.1 ms^{-1}. The desired temperature range for this test run was set to be between 1375 K (melting point of Mg_2Si) and 1683K (melting point of Si). The melting point of Si was set to be the upper bound to facilitate the suspension of Si nanoparticles without melting in the molten pool, which is said to enhance the thermoelectric

Table 3.1: First Run - Simulation Parameters - CFD

Input	Value	Unit
Material melting point	1375[46]	K
Solid thermal conductivity (k_p)	7[42]	$Wm^{-1}K^{-1}$
Liquid thermal conductivity (k_l)	5[42]	$Wm^{-1}K^{-1}$
Laser diameter (R)	0.3	mm

properties of the material on complete fabrication [54]. The maximum temperature attained in the molten pool for every tested parameter is depicted in Fig. 3.2.

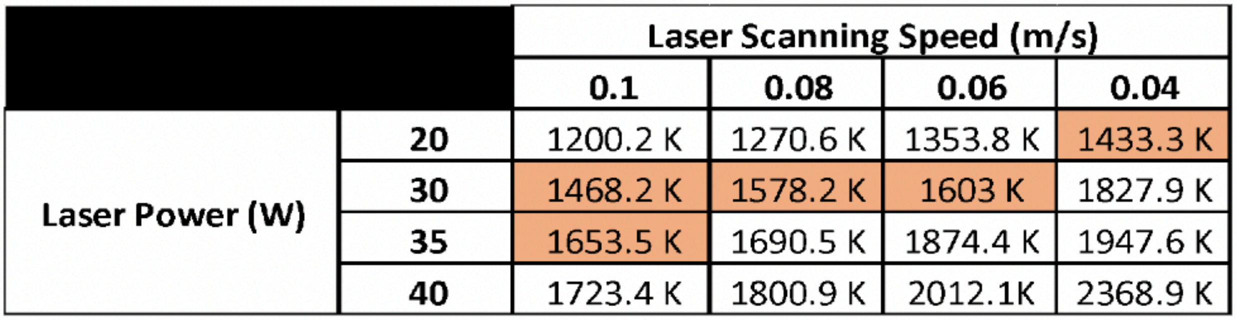

		Laser Scanning Speed (m/s)			
		0.1	0.08	0.06	0.04
Laser Power (W)	20	1200.2 K	1270.6 K	1353.8 K	1433.3 K
	30	1468.2 K	1578.2 K	1603 K	1827.9 K
	35	1653.5 K	1690.5 K	1874.4 K	1947.6 K
	40	1723.4 K	1800.9 K	2012.1K	2368.9 K

Figure 3.2: Maximum temperature in the molten pool for different processing conditions - First run

The highlighted temperatures in Fig. 3.2 are the temperatures that fall within the temperature bounds of 1375K and 1683K, and these process parameters were hence chosen to be the most favorable parameters for fabrication.

These chosen parameters with varying scan rates and laser powers were then tested for printing the Mg_2Si powder material using the OpenAdditive PANDA Selective Laser Melting equipment depicted in Fig. 3.3.

The printed components are depicted in Fig. 3.4 with a wide degree of balling, and key hole [55] effect visible as a result of the excessive Mg vaporization over the surface depending on the laser parameter and the localized melt pool temperature above its boiling point.

As visible from Fig. 3.4, evidently, the laser configuration with a power of 20W and a scan rate of 0.06m/s stands out as the most optimal among the alternatives. It exhibits markedly fewer visible indications of balling and porosity on the surface, signifying a minimized escape of volatile Mg during the interaction between the laser and the material, as the maximum temperature in the melt pool for this case is 1353K, which is less than the boiling point of Mg (1363K). Regarding the 30W laser, an increase in scan rate from 0.06 to 0.1m/s correlates

Figure 3.3: OpenAdditive PANDA SLM equipment

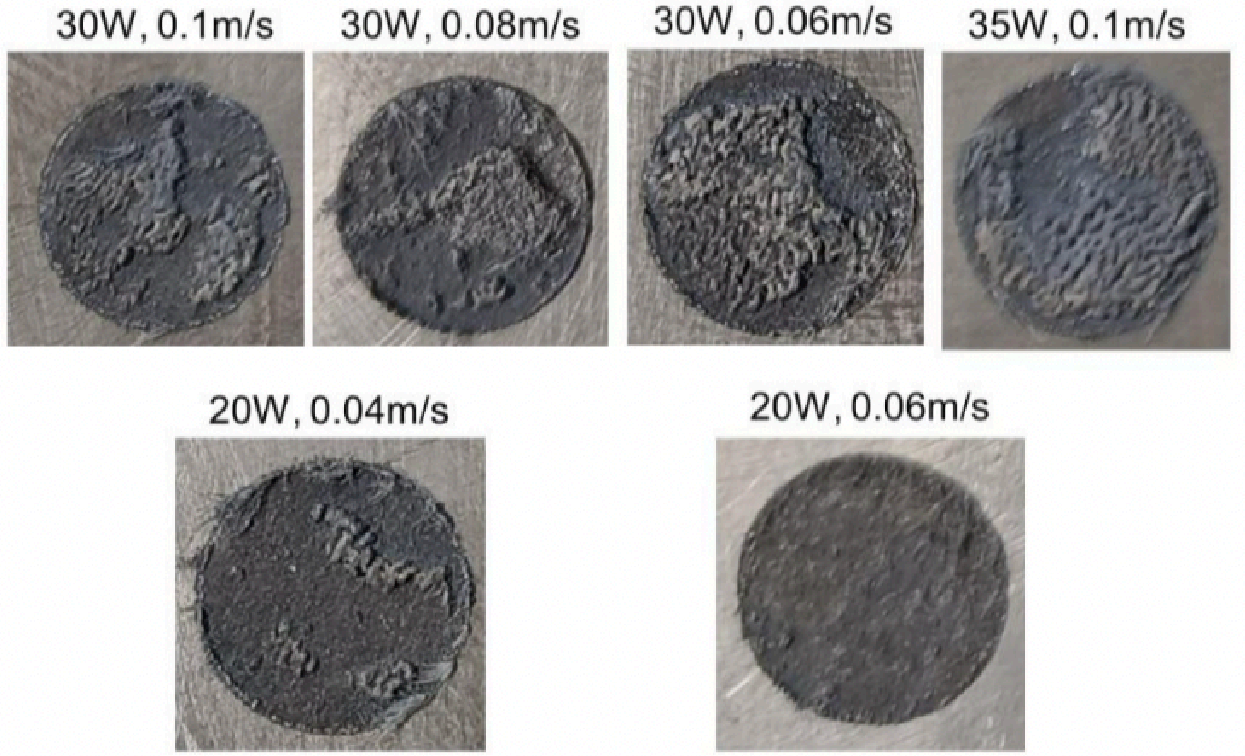

Figure 3.4: Zoomed-in pictures of the individual components showing the balling as a result of the respective laser parameter (Top View)

with a reduction in porosity. This reduction can be attributed to the corresponding decrease in the maximum melt pool temperature, dropping from approximately 1600K to around 1460K, as indicated by the data in Fig. 3.2. The Mg loss has been linked critically to the compound's stability, phase, and resulting thermoelectric properties [56, 57]. Based on the test runs the target melt pool temperature was set lower than Mg boiling point and close to the conventional sintering temperature to check its efficacy in preventing Mg loss. Another set of parameters was simulated and tested, as mentioned in the following section.

Second run - Thermally Favourable Process Parameters

The learnings from the first test were used to optimize the simulation parameters further to the ones depicted in Table 1. Notably, the sintering temperature was reduced from 1375K to 1173K(900°C[45]). Further, since the melt pool and surrounding areas of the powder bed are at a higher temperature, the solid and liquid thermal conductivity values were also reduced to match with their reported numbers at higher temperature [42, 43, 44] instead of the initially taken room temperature values. The complete set of parameters is depicted in Table 1. The test matrix of process parameters set for this run were laser powers of 10W-15W and scanning speeds ranging from 0.05m/s-0.2m/s. The desired temperature range for this test run was set to be between 1173K (Set sintering temperature) and 1363K (Boiling point of Mg). The maximum temperature attained in the molten pool for every tested parameter is depicted in Fig. 3.5.

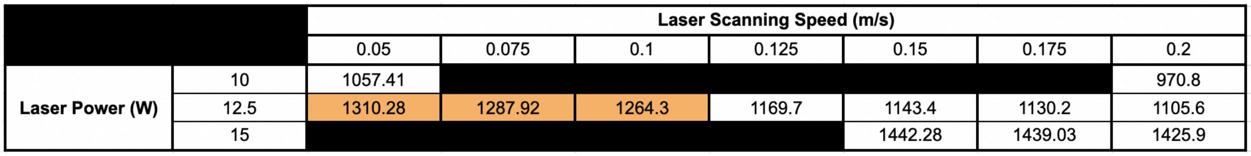

		Laser Scanning Speed (m/s)						
		0.05	0.075	0.1	0.125	0.15	0.175	0.2
Laser Power (W)	10	1057.41						970.8
	12.5	1310.28	1287.92	1264.3	1169.7	1143.4	1130.2	1105.6
	15					1442.28	1439.03	1425.9

Figure 3.5: Maximum temperature in the molten pool for different processing conditions - Second run

The highlighted temperatures in Fig. 3.5 are the temperatures that fall within the temperature bounds of 1173K and 1363K, and these process parameters were hence chosen to be the most favorable parameters for fabrication. The maximum temperature obtained for the lowest scanning speed of 0.05 m/s in the 10W test was 1057.41K which is below the sintering temperature of 1173K. Hence, further simulations were not run for higher scanning speeds as the meltpool temperatures would only decrease further due to a decrease in the energy density. Similarly, tests were not run for lower scanning speeds in the 15W test case as the high scanning speeds gave a set of temperatures above 1400K, which is well above the boiling point of Mg. These parameters with varying scan rates and laser powers were then again tested for printing the Mg_2Si powder material. The result from the print done under processing conditions of 12.5W and 0.05 m/s is depicted in Fig. 3.6. which shows the x-ray diffraction pattern obtained from the precursor powder and the laser-printed sample (image of the printed sample inset). The precursor powder peaks could be indexed to Mg_2Si (ICSD collection code 122860) with traces of elemental Mg and MgO. The Mg_2Si phase in the laser-printed component is conserved to some extent with visible signs of material degradation, which has aggravated the elemental Si, and MgO content as observable from the relative intensity of the labeled peaks. Further, since the elemental Mg content is visibly unchanged (unchanged peak intensity for the Mg), it may be concluded that the reduction in the melt pool temperature successfully curtailed the Mg vaporization. Although, Mg_2Si material degradation at high temperatures in the presence of traces of oxygen is a known phenomenon [45, 58] which is observed here.

As visible from Fig. 3.6, an intact and solid printed part without significant balling or porosity as compared to the test run has been obtained. This could be attributed to the lower melt pool temperatures attained with the refined process parameters, which are within the defined temperature bounds. Hence, it's clear that these parameters were successful in

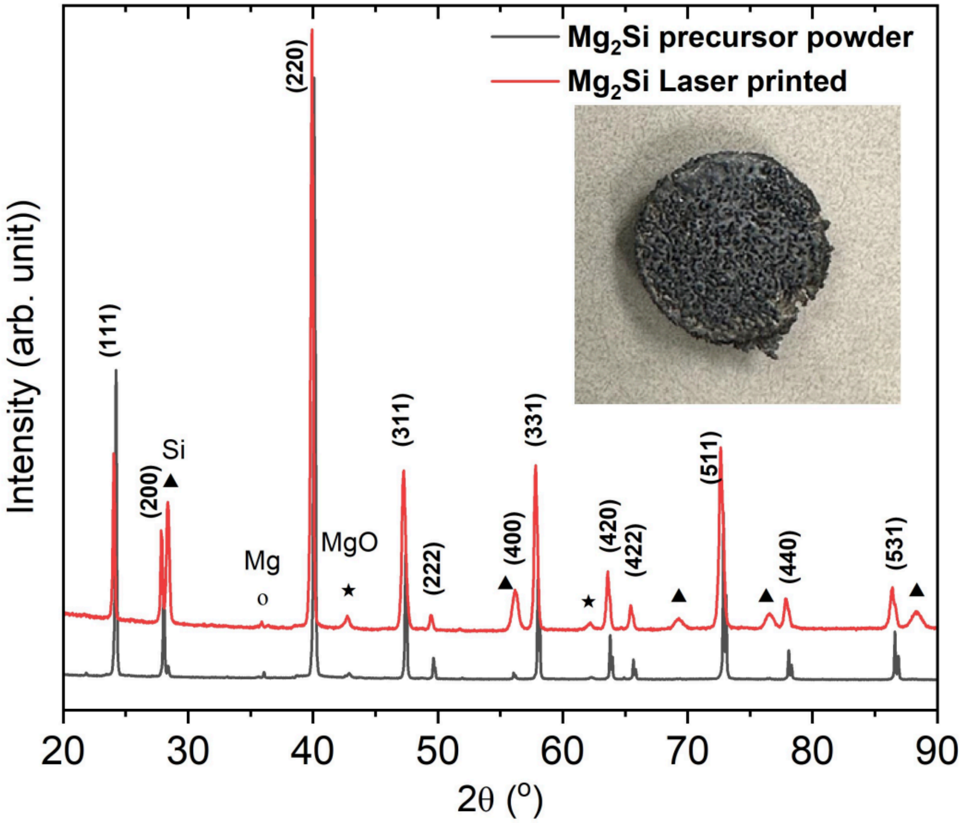

Figure 3.6: XRD comparison of the precursor powder and the printed Mg2Si material with laser parameters - Q = 12.5W; U_b = 0.05 m/s

preventing the Mg evaporation, and a relatively denser Mg_2Si component could be obtained with laser printing, which also further validates the developed code.

Melt-Pool Thermal Kinetics - Temperature

Analyzing the thermal meltpool kinetics was essential to understanding the effects of laser power and speed on the meltpool development. The meltpool temperature profiles obtained for a select set of parameters by keeping the laser power constant and increasing the scanning speed are depicted in Fig. 3.7. As depicted, when the scanning speed is increased by keeping the laser power constant, the peak temperature in the molten pool decreases. It can also be observed that the molten pool tail observed due to the movement of the laser becomes more prominent as the scanning speed increases.

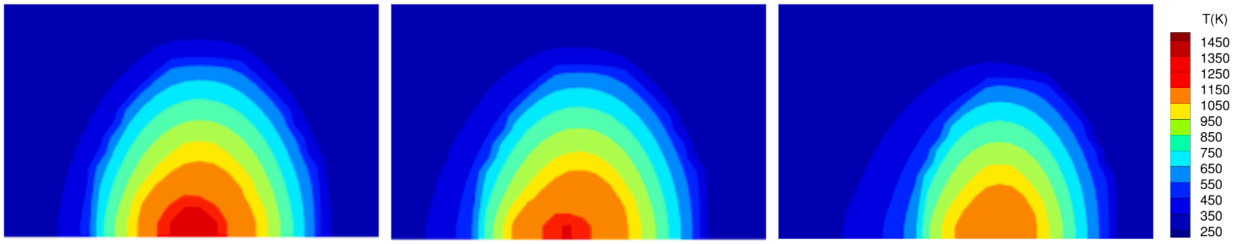

a) 12.5W, 0.05m/s b) 12.5W, 0.1m/s c) 12.5W, 0.2m/s

Figure 3.7: Top view of the melt pool profiles with increasing scanning speeds

The influence of keeping the scan speed constant, and increasing the power from 10W-15W is depicted in Fig. 3.8.

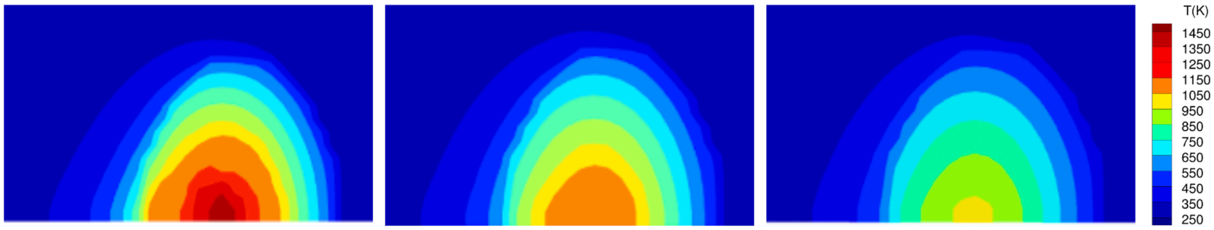

a) 15W, 0.2m/s b) 12.5W, 0.2m/s c) 10W, 0.2m/s

Figure 3.8: Top view of the meltpool profiles with increasing laser powers

As depicted in Fig. 3.8, the peak temperature in the melt pool increases as expected with an increase in power, which also results in an increase in the molten pool size. The radius of the meltpool for the desired parameters was found to vary from about 20μm to 40μm as the scanning speed decreased from 0.1m/s to 0.05m/s at a laser power of 12.5W. Hence, it's important to adjust the layer height and hatch spacing for each processing condition to facilitate proper adhesion between layers to fabricate these thermoelectric powders efficiently. These temperature profiles were used to calculate the temperature gradient and the cooling rate in the direction parallel to the laser path, as these parameters affect the microstructure growth and are used as input for the phase field simulation.

The following formula used in reference [59] was used to calculate the temperature gradient:

$$G = \frac{T_{max} - T_l}{r} \tag{3.1}$$

where T_{max} is the maximum temperature in the melt pool, T_l is the liquidus temperature set as the sintering temperature in this case, and r is the distance between the location of the maximum temperature and the chosen position along the liquidus line (boundary of the melt pool). The solidification rate R can be calculated with the geometrical relationship as mentioned in the reference [48]:

$$R = U_b \cos(\alpha) \tag{3.2}$$

where U_b is the beam scanning speed, and α is the angle between the normal to the S/L interface and the beam scanning direction. Since the temperature gradient and solidification rate are calculated in the direction parallel to the laser path in this study, α is taken as 0 degrees which makes the solidification rate take the same value as the scanning speed. The cooling rate $\dot{T}$ was calculated by taking the product of the temperature gradient G and the solidification rate R[48]:

$$\dot{T} = GR \tag{3.3}$$

The calculated temperature gradients and cooling rates for the three most favorable parameters are depicted below in Fig. 3.9. It is worth noting that the cooling rate increases with an increase in scanning speed while the temperature gradient does not change drastically as the range of molten pool sizes and temperatures for these parameters are not very wide, as depicted in Fig. 3.5.

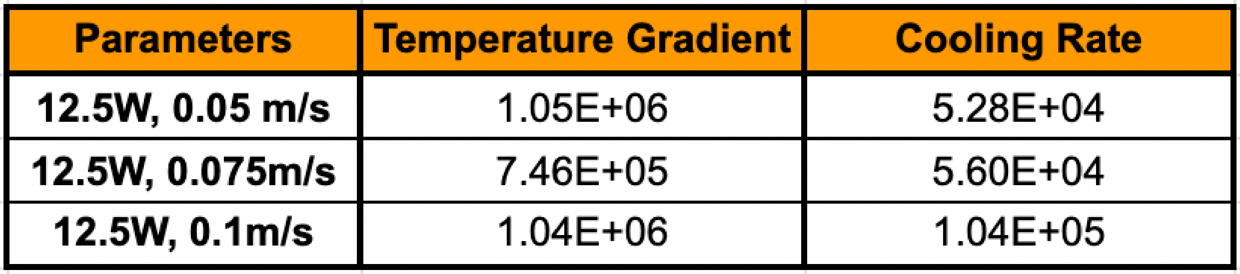

Parameters	Temperature Gradient	Cooling Rate
12.5W, 0.05 m/s	1.05E+06	5.28E+04
12.5W, 0.075m/s	7.46E+05	5.60E+04
12.5W, 0.1m/s	1.04E+06	1.04E+05

Figure 3.9: Calculated temperature gradients and cooling rates

Melt-Pool Thermal Kinetics - Velocity and Spatter

The flow circulations within the molten pool in Selective Laser Melting (SLM) arise from multiple factors, notably the temperature gradient induced by the movement of the laser, as depicted in Fig. 3.7. This gradient generates an uneven distribution of surface tension across the molten pool due to its inverse correlation with temperature. This phenomenon, known as Marangoni convection, intensifies the unbalanced surface tension within the molten pool. Additionally, buoyant forces present in the molten pool further contribute to the initiation of convective currents within the liquid melt. As a result, the lower temperature at the outer periphery of the molten pool induces higher surface tension, attracting the liquid melt towards this region. Simultaneously, buoyant forces drive a flow pattern from the bottom to the top of the molten pool, reinforcing the observed circulatory motion as depicted in Fig. 3.10.

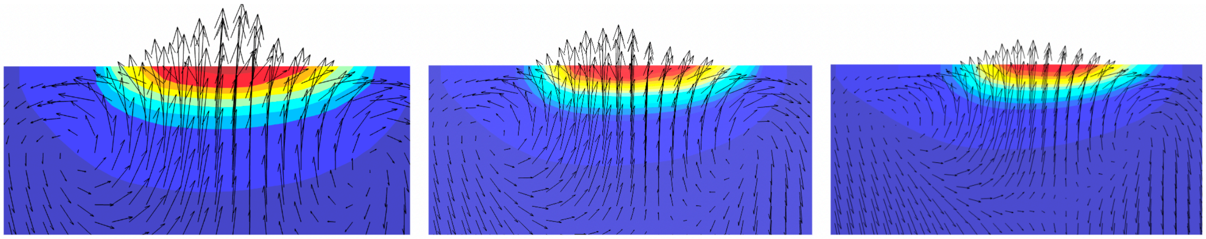

a) 12.5W, 0.05m/s b) 12.5W, 0.1m/s c) 12.5W, 0.2m/s

Figure 3.10: Cross-sectional view of the melt pool profiles with increasing scanning speeds

Observations from Fig. 3.10 highlight the amplification of circulations and convection within the molten pool as the energy density (represented by Laser Power/Laser Scanning Speed) increases. This is evident from the intensified velocity streamlines delineated within the molten pool. Additionally, noteworthy from Fig. 3.10 is the correlation between scanning speed, power, and the depth of the molten pool. A higher scanning speed, while maintaining constant power, leads to a reduction in the molten pool depth. This alteration influences the temperature gradient within the molten pool, subsequently impacting the convective currents present in the liquid melt.

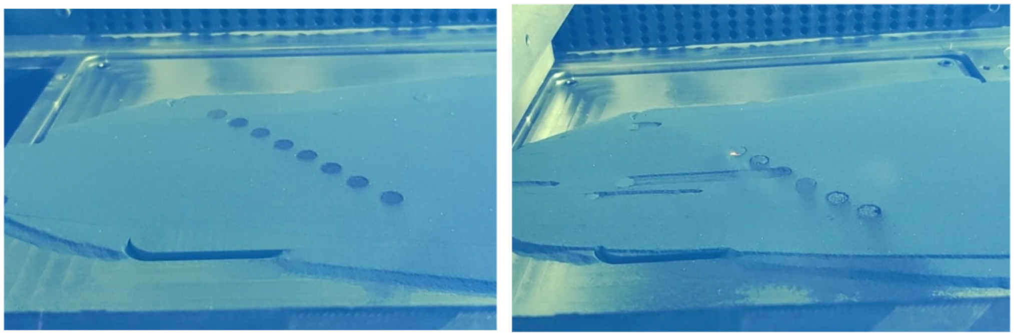

(a) Start of Print

(b) Midway of print

Figure 3.11: Visible spatter of Mg_2Si during the print

The convection patterns depicted in Fig. 3.10 also help explain the spatter[60] of powder observed on the sides of the print bed during the experimental testing, as depicted in Fig. 3.11. As visible from Fig. 3.10, the velocity streamlines resulting due to the Marangoni convection points outwards from the molten pool, which can result in the ejection of liquid melt or unmelted powders as observed in Fig. 3.11. In materials like Mg_2Si with a relatively low density, the interplay between temperature gradients induced by the laser and surface tension variations leads to intensified convective currents. Simultaneously, the presence of recoil pressure[60], especially pronounced due to the vapor plume as depicted in Fig. 3.12 resulting from the evaporation of Mg in Mg_2Si, becomes a contributing factor to the spatter.

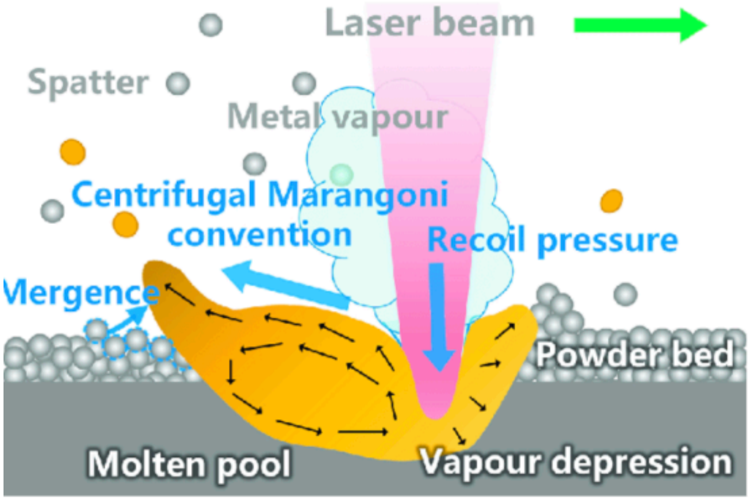

Figure 3.12: Marangoni convection, recoil pressure, and its effect on spatter[1]

This recoil pressure emerges as the high-power laser vaporizes the material, creating a high-pressure vapor plume that exerts a force on the molten pool, potentially causing splattering or spatter. Understanding and managing these combined effects of Marangoni convection and recoil pressure, especially concerning materials with unique characteristics like Mg_2Si, are crucial in controlling spatter and optimizing the additive manufacturing process for desired outcomes.

3.0.2 Phase Field Simulation Results

Code Validation

Directional solidification of dendrites is expected to happen by the edges of the molten pool[61] in the direction of the temperature gradient due to energetically favorable heterogeneous nucleation that tends to happen by the S/L interface. Since the met pool radius varies from $20\mu m$ to $40\mu m$ for this material based on the melt pool analysis, a square computational domain of size $10\mu m \times 10\mu m$ was chosen as depicted in Table. 2.2 to emulate the dendrite growth by the edges of the molten pool. Additionally, a small computational domain size also helped reduce the computational time.

The computational domain is initialized with a small solid nucleus with a diameter of $0.35\mu m$. Figure 3.15 shows the evolution of the microstructure during solidification from the predefined solid nucleus for a case with the laser power set to 12.5W and scanning speed set to 0.1m/s. As the solidification time increased, it can be seen that the dendrites branched out into the molten pool along the applied temperature gradient in the X direction, as depicted in Fig. 3.15. It can be noted that, with the passage of time, the dendrites branch out from the primary dendrites to form secondary and tertiary dendrites. And, the solute concentration ratio, as shown in Fig. 3.16, also follows the expected trend. The solute concentration ratio is defined as:

$$ConcentrationRatio = \frac{c}{{c_l}^o} \tag{3.4}$$

where ${c_l}^o$ is $\frac{c_\infty}{k}$. The concentration c of the completely solidified phase (region with $\phi = 1$ in Fig. 3.15) and the liquid phase (region with $\phi =$ -1 in Fig. 3.15) ahead of the interface should be unchanged at the initial solute concentration of c_∞[62] which makes the concentration ratio in these regions equal to k(k = 0.3 as shown in Table 2.2). This aligns well with the modeling result as shown in Fig. 3.16. It should also be noted in Fig. 3.16 that the solute concentration is high in the interdendritic region as the solute is ejected from the advancing solid interface to the liquid owing to the solid's lower solute solubility compared to the liquid [62].

According to the theory of solidification, the concentration c ahead of the interface is high at c_∞/k and decays down to c_∞ like depicted in Fig. 3.13 as we move into the liquid farther away from the interface [62]. The same can be observed in the modeled results as seen in

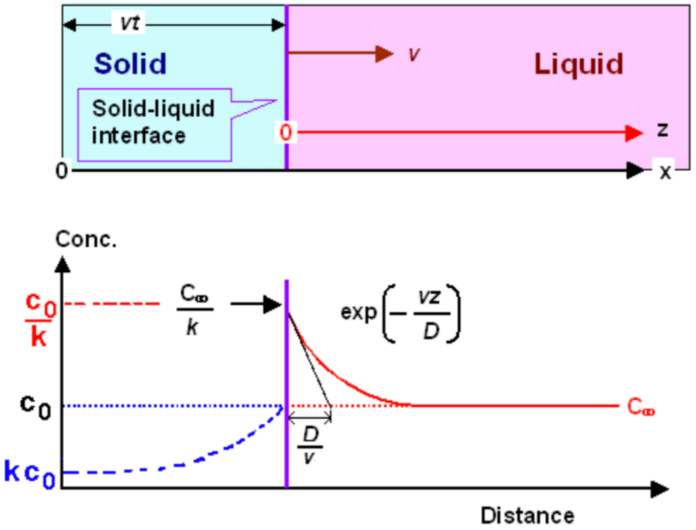

Figure 3.13: Solute concentration variation at the S/L interface (Expected)

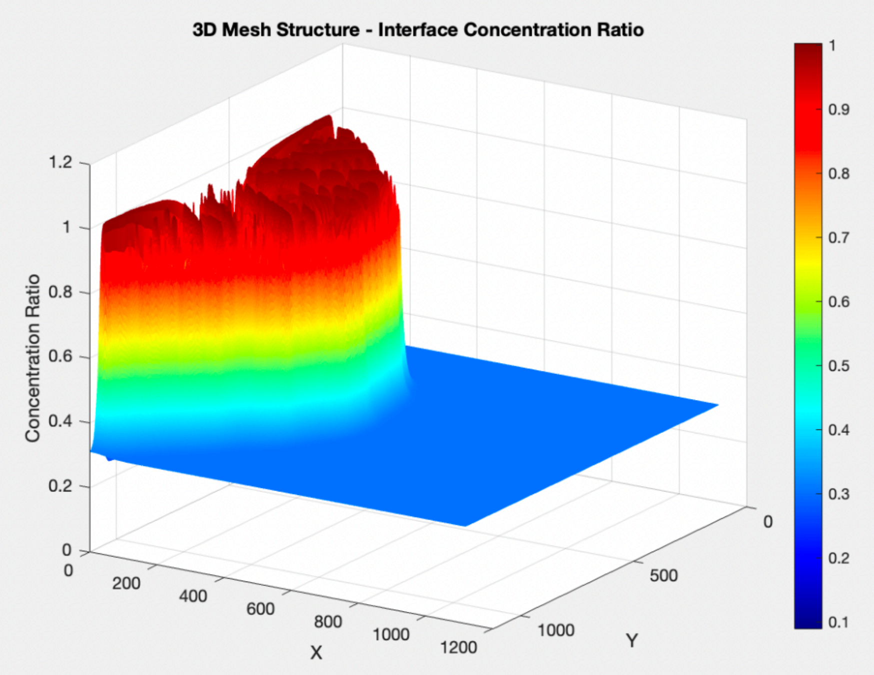

Figure 3.14: Variation of concentration ratio ahead of the S/L interface

Fig.3.16. This phenomenon is clearly visible in the 3D graph generated for the concentration ratio variation as depicted in Fig. 3.14.

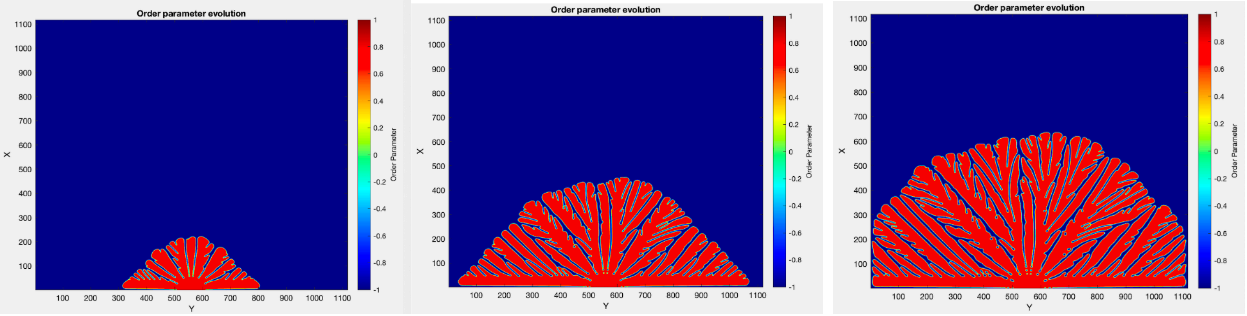

(a) t = 0.016ms (b) t = 0.038ms (c) t = 0.055ms

Figure 3.15: Microstructure evolution - Q = 12.5W, U_b = 0.1m/s

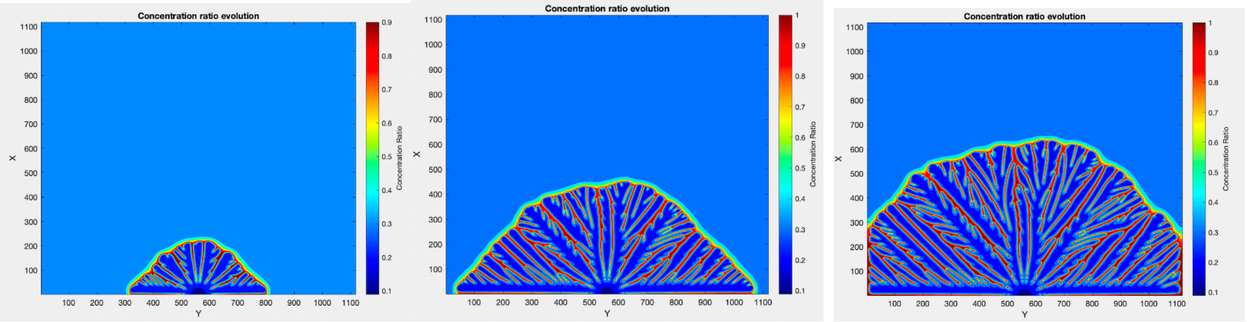

(a) t = 0.016ms (b) t = 0.038ms (c) t = 0.055ms

Figure 3.16: Concentration ratio ($\frac{c}{{c_l}^o}$) evolution - Q = 12.5W, U_b = 0.1m/s

Additionally, the Secondary Dendritic Arm Spacing (SDAS) was measured and compared with the analytical values. The analytical SDAS was calculated with the analytical model proposed by Kurz and Fisher [63] as given below:

$$\lambda = 4.3(k\Delta T_o D\Gamma)^{\frac{1}{4}} R^{\frac{-1}{4}} G^{\frac{-1}{2}} \tag{3.5}$$

where λ is the SDAS in μm, k is the partition coefficient, $\Delta T_o = |m|c_\infty(1-k)/k$, Γ is the Gibbs Thomson coefficient (Kmm), D is the diffusion coefficient (mm^2s^{-1}), R is the solidification rate (mms^{-1}), and G is the temperature gradient (K/mm). ImageJ was used to measure SDAS from the simulated result for the case depicted in Fig. 3.15. The average value of SDAS obtained from the simulated results was 0.012 ± 0.0015 μm while the analytical value obtained was approximately equal to 0.00457 μm. The variation observed can most likely be attributed to the simulation parameters like the low Gibbs-Thomson coefficient value approximated for the material[52], which is still not available in the literature and needs further research. Nevertheless, the values are still comparable, and that further validates the code.

Microstructural Analysis

Correlation with scanning speed

The temperature gradient and solidification rate obtained from the CFD-based simulation for the favorable process parameters were used as input parameters in the phase field model to understand the correlation between the process parameters and the microstructure. The temperature gradient and the solidification rate corresponding to the scanning speeds of 0.05m/s and 0.1m/s at a laser power of 12.5W were used to understand the influence of increasing scanning speed on the microstructure. The results from this run after 0.038ms are depicted in Fig. 3.17. It can be observed that, with the increase in scanning speed (also an increase in cooling rate), there is a visible reduction in the dendrite tip radius due to increased branching near the tips. There is also a reduction in secondary and tertiary dendrite branching from the sides of the primary dendrite axes, which reduces the primary interdendritic spacing (PDAS). The average PDAS was calculated using ImageJ, and with an increase in scanning speed, the PDAS was found to reduce from 0.458 μm to 0.348 μm. Hence, the simulated microstructure follows the general rule of finer microstructure (lower PDAS) with an increase in scanning speed and cooling rate.

The interdendritic regions are solute-rich, as depicted in Fig. 3.16, and these are the regions

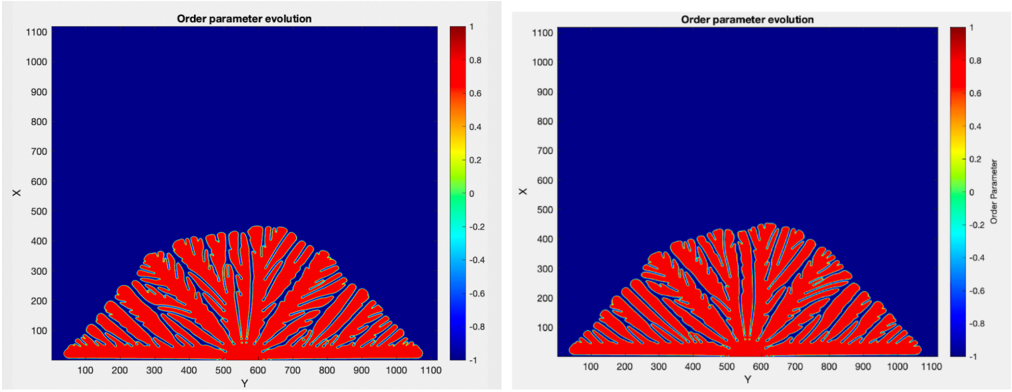

(a) Q = 12.5W, U_b = 0.05m/s (b) Q = 12.5W, U_b = 0.1m/s

Figure 3.17: Microstructure variation with changing scanning speed (t=0.038ms)

that solidify in the end. Hence, an increase in the fraction of interdendritic regions would decrease the compositional and phase homogeneity of the material, which could alter the thermoelectric properties of Mg_2Si. This correlation requires more experimental data for validation with the microstructural and phase analysis with respect to the thermoelectric properties. As discussed in this section, the processing parameters can be optimized to enable efficient Selective Laser Melting fabrication of thermoelectric powders.

Influence of perturbation

Within solidification kinetics, inducing side branching through interface perturbations holds significant potential for altering microstructures. This comparative analysis scrutinizes simulations with and without these perturbations, aiming to unveil their distinct effects on dendritic growth. The deliberate introduction of perturbations at the solid-liquid interface serves as a mechanism to manipulate side branching during solidification. This discussion dissects resultant microstructural disparities, emphasizing the nuanced influence of perturbations on dendrite morphology and solidification dynamics.

The temperature gradient and solidification rate corresponding to the processing parameters of a laser power of 12.5W and a scanning speed of 0.1 m/s at t = 0.038ms were used for the microstructure comparison with and without the addition of perturbation as depicted in Fig. 3.18.

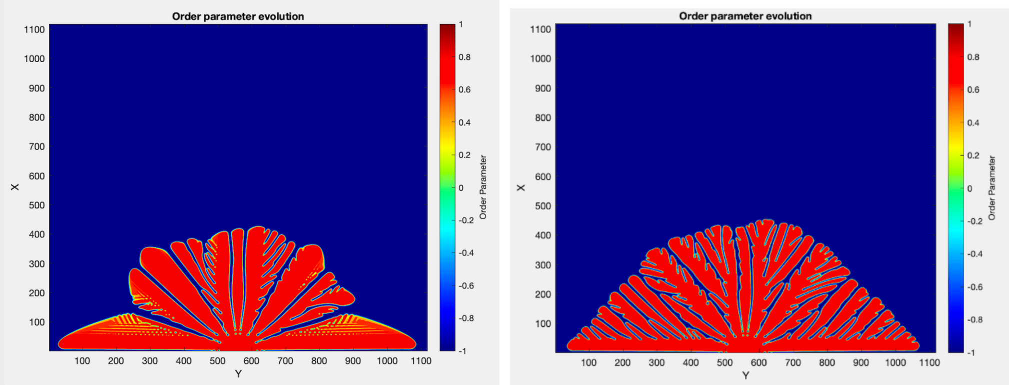

(a) Without perturbation (b) With perturbation

Figure 3.18: Effect of perturbation on the microstructure (Q = 12.5W, U_b = 0.1m/s, t=0.038ms)

The influence of the perturbation becomes evident upon comparing the side branching observed in primary dendrites, as depicted in Fig. 3.18a. Removal of the perturbation notably diminishes this branching effect. Localized at the solid-liquid interface, the perturbation serves to destabilize grain boundaries within primary dendrites, fostering the development of secondary and tertiary dendrites, as illustrated in Fig. 3.18b. Moreover, the introduction of noise via the perturbation reduces the dendrite tip radius, encouraging branching at these sites. The absence of such perturbations leads to inadequate side branching, resulting in reduced solidified area due to inefficient filling of spaces between primary dendrites. This underscores the perturbation's crucial role in facilitating secondary and tertiary dendrite formation, optimizing solidification efficiency.

Influence of the strength of anisotropy (ϵ_4)

In phase-field simulations, the anisotropy coefficient (ϵ_4) serves as a key determinant of directional preferences in surface tension, interface thickness, and dynamic behaviors. ϵ_4 signifies the degree of anisotropy governing surface energy variations, and influences preferred growth directions during crystalline evolution. Additionally, it modulates interface thickness, highlighting orientation-specific characteristics. This section examines the impact of varying (ϵ_4) on microstructure evolution, unraveling its role in shaping resultant microstructural features.

The temperature gradient and solidification rate corresponding to the processing parameters of a laser power of 12.5W and a scanning speed of 0.1 m/s at t = 0.055ms were used for the microstructure comparison with a changing ϵ_4 as depicted in Fig. 3.19.

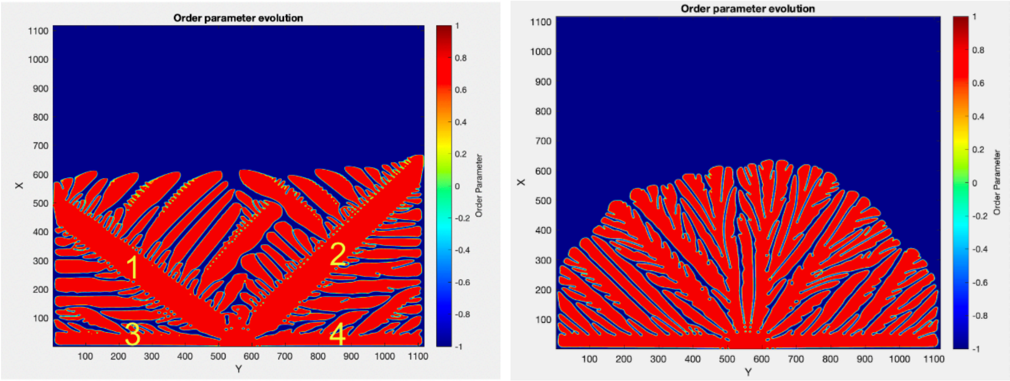

(a) $\epsilon_4 = 0.02$

(b) $\epsilon_4 = 0.002$

Figure 3.19: Effect of the strength of anisotropy (ϵ_4) on the microstructure (Q = 12.5W, U_b = 0.1m/s, t=0.055ms)

When augmenting the strength of anisotropy by an order of magnitude, from 0.002 to 0.02 (as illustrated in Fig. 3.19), noticeable alterations occurred in the preferred growth orientations of dendrites. Referring to Eq. 2.39, a presumed four-fold anisotropy was considered. The increase in ϵ_4 accentuated the four-fold anisotropic nature of dendritic morphology, visibly evident in Fig. 3.19a, where four distinctly labeled primary dendrites emanate from the nucleus. This heightened anisotropy manifests a clearer preference for specific crystallographic orientations, markedly influencing the resulting dendritic growth patterns.

Chapter 4

Conclusions And Future Work

This work is likely the first demonstration of the Mg_2Si fabrication using Selective Laser Melting (SLM) along with the process's numerical CFD analysis. A three-dimensional numerical model of the molten pool was developed, focusing on varying laser powers and scanning speeds to derive detailed temperature profiles and optimize process parameters. The range in which the melt pool temperature lies with respect to the boiling point of Mg and the sintering temperature of Mg_2Si was found to be crucial to preserving the phase and structural integrity of the printed component.

Further, the thermal data from the CFD model was input to a phase field analysis aimed at understanding the impact of processing parameters on dendritic growth during solidification. The effect of increasing the laser scanning speed, hence a higher cooling rate, was observed to result in a finer microstructure with reduced Primary Dendrite Arm Spacing (PDAS). Thus, tailoring the microstructure is possible to suit the application. The possible microstructural features were successfully simulated with an indication of solute concentration variation in different regions. The efficacy of the modeled CFD data to depict the solidification kinetics and melt pool temperature profiles converging into dendritic growth was tested successfully. Additionally, investigating the impact of certain numerical parameters on the microstructure involved deliberate modifications in factors like perturbation intensity and the magnitude of surface tension anisotropy. These intentional adjustments were made to comprehensively analyze and understand the influence of these variables on the final microstructural outcomes.

Furthermore, the study opens the scope for an extensive material characterization of the fabricated Mg_2Si components. This would entail a thorough examination of the microstructure and functional properties to understand how the various processing conditions influence it and how accurately it fits with the phase field modeled data. For instance, the secondary phases, Si and MgO, present in the laser-printed Mg_2Si sample could act as the perturbations leading to variation in the dendritic growth. At the same time, it is also probable that the anisotropy may change with their presence, leading to a different microstructure. The relationship between fabrication conditions, microstructural characteristics, and the resulting functional properties of Mg_2Si may be established based on the experiment-model data correlation to advance the manufacturing methods involving laser melting. To optimize the developed code, conducting experimental trials aimed at precise prediction of essential material properties, such as Gibbs Thomson's coefficient, would significantly enhance the accuracy of inputs into the model. Furthermore, enhancing the computational efficiency by incorporating parallelization techniques stands to decrease processing time notably. This improvement would not only streamline testing procedures but also would lay the groundwork for more efficient computational analyses

Bibliography

[1] Jie Yin, Wang Dengzhi, Liangliang Yang, Huiliang Wei, Peng Dong, Linda Ke, Guoqing Wang, Haihong Zhu, and Xiaoyan Zeng. Correlation between forming quality and spatter dynamics in laser powder bed fusion. *Additive Manufacturing*, 31:100958, 01 2020.

[2] Ian Campbell, Olaf Diegel, Joseph Kowen, and Terry T. Wohlers. Wohlers report 2018: 3d printing and additive manufacturing state of the industry: Annual worldwide progress report. 2017.

[3] Ana Vafadar, Ferdinando Guzzomi, Alexander Rassau, and Kevin Hayward. Advances in metal additive manufacturing: A review of common processes, industrial applications, and current challenges. *Applied Sciences*, 11(3), 2021.

[4] Takayoshi Nakano. Selective laser melting. *Multi-dimensional Additive Manufacturing*, 2020.

[5] Debdatta Ratna. Chapter 2 - properties and processing of thermoset resin. In Debdatta Ratna, editor, *Recent Advances and Applications of Thermoset Resins (Second Edition)*, pages 173–292. Elsevier, second edition edition, 2022.

[6] Pacurar Razvan and Pacurar Ancuta. Applications of the selective laser melting technology in the industrial and medical fields. In Igor V Shishkovsky, editor, *New Trends in 3D Printing*, chapter 8. IntechOpen, Rijeka, 2016.

[7] Yohann Thimont and Saniya Leblanc. The impact of thermoelectric leg geometries on thermal resistance and power output. *Journal of Applied Physics*, 126:095101, 09 2019.

[8] Yu Mao, Yan Yonggao, Keping Wu, Hongyao Xie, Zekun Xiu, Jihui Yang, Qingjie Zhang, Ctirad Uher, and Xinfeng Tang. Non-equilibrium synthesis and characterization of n-type bi 2 te 2.7 se 0.3 thermoelectric material prepared by rapid laser melting and solidification. *RSC Adv.*, 7:21439–21445, 04 2017.

[9] Yan Yonggao, Hongquan Ke, Jihui Yang, Ctirad Uher, and Xinfeng Tang. Fabrication and thermoelectric properties of n-type cosb2.85te0.15 using selective laser melting. *ACS applied materials interfaces*, 10, 04 2018.

[10] Haidong Zhang, Dean Hobbis, George S. Nolas, and Saniya LeBlanc. Laser additive manufacturing of powdered bismuth telluride. *Journal of Materials Research*, 33(23):4031–4039, 2018.

[11] Jianxu Shi, Hualing Chen, Shuhai Jia, and Wanjun Wang. 3d printing fabrication of porous bismuth antimony telluride and study of the thermoelectric properties. *Journal of Manufacturing Processes*, 37:370–375, 2019.

[12] Gagan K. Goyal and T. Dasgupta. Fabrication and testing of mg2si1-xsnx based thermoelectric generator module. *Materials Science and Engineering: B*, 272:115338, 2021.

[13] Gagan Goyal and Titas Dasgupta. Generic approach for contacting thermoelectric solid solutions: Case study in n- and p-type mg2si0.3sn0.7. *ACS applied materials interfaces*, 13, 04 2021.

[14] Xinzhi Wu, Yangjian Lin, Chengyan Liu, Zhijia Han, Huan Li, Yupeng Wang, Feng Jiang, Kang Zhu, Binghui Ge, and Weishu Liu. Interface engineering boosting high power density and conversion efficiency in mg2sn0.75ge0.25-based thermoelectric devices. *Advanced Energy Materials*, 13(32):2301350.

[15] Julia Camut, Pawel Ziolkowski, Prasanna Ponnusamy, Christian Stiewe, Eckhard

Mueller, and Johannes de Boor. Efficiency measurement and modeling of a high-performance mg2(si,sn)-based thermoelectric generator. *Advanced Engineering Materials*, 25(1):2200776.

[16] Bo Zhang, Lei Zuo, Gaosheng Fu, Xiaoya Shi, Mahder Tewolde, Jon Longtin, Yikai Chen, and Sanjay Sampath. Thermoelectric properties of magnesium silicide prepared by thermal spraying. 07 2012.

[17] Q.D. Qin, Yu Zhao, W. Zhou, and P.J. Cong. Effect of phosphorus on microstructure and growth manner of primary mg2si crystal in mg2si/al composite. *Materials Science and Engineering: A*, 447:186–191, 02 2007.

[18] Chunlei Li, Yuying Wu, and Xiangfa Liu. Morphological evolution and growth mechanism of primary mg 2si phase in al–mg 2si alloys. *Acta Materialia - ACTA MATER*, 59:1058–1067, 02 2011.

[19] Nader Farahi, Sagar Prabhudev, Gianluigi Botton, J. Salvador, and Holger Kleinke. Nano- and microstructure engineering: An effective method for creating high efficiency magnesium silicide based thermoelectrics. *ACS Applied Materials Interfaces*, 8, 11 2016.

[20] Ahmed Hussein, Chunze Yan, and Richard Everson. Finite element simulation of the temperature and stress fields in single layers built without-support in selective laser melting. *Materials Design*, 52, 12 2013.

[21] D. Zhang, Q. Cai, J. Liu, L. Zhang, and Ruidi Li. Select laser melting of w-ni-fe powders: Simulation and experimental study. *International Journal of Advanced Manufacturing Technology*, 51:649–658, 11 2010.

[22] Bin Xiao and Yuwen Zhang. Marangoni and buoyancy effects on direct metal laser

sintering with a moving laser beam. *Numerical Heat Transfer Part A-applications - NUMER HEAT TRANSFER PT A-APPL*, 51:715–733, 04 2007.

[23] J.P. Kruth, L. Froyen, J. Van Vaerenbergh, P. Mercelis, M. Rombouts, and B. Lauwers. Selective laser melting of iron-based powder. *Journal of Materials Processing Technology*, 149(1):616–622, 2004. 14th International Symposium on Electromachining (ISEM XIV).

[24] Carolin Körner, Elham Attar, and Peter Heinl. Mesoscopic simulation of selective beam melting processes. *Journal of Materials Processing Technology*, 211:978–987, 06 2011.

[25] Saad Khairallah and Andy Anderson. Mesoscopic simulation model of selective laser melting of stainless steel powder. *Journal of Materials Processing Technology*, 214:2627–2636, 11 2014.

[26] Heng Gu, Chao Wei, Lin Li, Quanquan Han, Rossitza Setchi, Michael Ryan, and Qian Li. Multi-physics modelling of molten pool development and track formation in multi-track, multi-layer and multi-material selective laser melting. *International Journal of Heat and Mass Transfer*, 151:119458, 2020.

[27] Yongjia Wu, Kan Sun, Shifeng Yu, and Lei Zuo. Modeling the selective laser melting-based additive manufacturing of thermoelectric powders. *Additive Manufacturing*, 37:101666, 2021.

[28] H. Yin and S.D. Felicelli. Dendrite growth simulation during solidification in the lens process. *Acta Materialia*, 58(4):1455–1465, 2010.

[29] Bing hui Tian, Meng wu Wu, Ang Zhang, Zhipeng Guo, and Shoumei Xiong. Phase-field modeling of dendritic growth of magnesium alloys with a parallel-adaptive mesh refinement algorithm. *China Foundry*, 18:541 – 549, 2021.

[30] Blas Echebarria, Roger Folch, Alain Karma, and Mathis Plapp. Quantitative phase field model of alloy solidification. *Physical review. E, Statistical, nonlinear, and soft matter physics*, 70:061604, 01 2005.

[31] Blas Echebarria, Alain Karma, and Sebastian Gurevich. Onset of sidebranching in directional solidification. *Phys. Rev. E*, 81:021608, Feb 2010.

[32] D. Tourret and A. Karma. Growth competition of columnar dendritic grains: A phase-field study. *Acta Materialia*, 82:64–83, 2015.

[33] Fei Wang, Alexander Matz, Oleg Tschukin, Johann Heimann, Bettina Matz Mocker, Britta Nestler, and Norbert Jost. Numerical and experimental investigations on the growth of the intermetallic mg 2 si phase in mg infiltrated si-foams: Numerical and experimental investigations on the growth.... *Advanced Engineering Materials*, 19:1700063, 04 2017.

[34] V.R. Voller, A.D. Brent, and C. Prakash. The modelling of heat, mass and solute transport in solidification systems. *International Journal of Heat and Mass Transfer*, 32(9):1719–1731, 1989.

[35] Radyadour Kh. Zeytounian. Joseph boussinesq and his approximation: a contemporary view. *Comptes Rendus Mécanique*, 331(8):575–586, 2003.

[36] G.R. Hadley. Thermal conductivity of packed metal powders. *International Journal of Heat and Mass Transfer*, 29(6):909–920, 1986.

[37] Michael Carter, Ahmed El-Desouky, Matthieu Andre, Philippe Bardet, and Saniya Leblanc. Pulsed laser melting of bismuth telluride thermoelectric materials. *Journal of Manufacturing Processes*, 43:35–46, 07 2019.

[38] S. K. Wang. Weld pool convection and its effect. 2013.

[39] Suhas V Patankar. *Numerical heat transfer and fluid flow.* Series on Computational Methods in Mechanics and Thermal Science. Hemisphere Publishing Corporation (CRC Press, Taylor & Francis Group), 1980.

[40] Bram van Leer. Towards the ultimate conservative difference scheme. ii. monotonicity and conservation combined in a second-order scheme. *Journal of Computational Physics*, 14:361–370, 03 1974.

[41] Henk Kaarle Versteeg and Weeratunge Malalasekera. *An introduction to computational fluid dynamics - the finite volume method.* Addison-Wesley-Longman, 1995.

[42] Masayasu Akasaka, Tsutomu Iida, Atsunobu Matsumoto, Kohei Yamanaka, Yoshifumi Takanashi, Tomohiro Imai, and Noriaki Hamada. The thermoelectric properties of bulk crystalline n- and p-type mg2si prepared by the vertical bridgman method. *Journal of Applied Physics*, 104:013703 – 013703, 08 2008.

[43] Richard J. LaBotz and Donald R. Mason. The thermal conductivities of mg2si and mg2ge. *Journal of The Electrochemical Society*, 110(2):121, feb 1963.

[44] Nikhil Satyala and Daryoosh Vashaee. Modeling of thermoelectric properties of magnesium silicide (mg 2 si). *Journal of Electronic Materials*, 41:1785–1791, 02 2012.

[45] Kunal Mitra, Gagan Goyal, Ekashmi Rathore, Kanishka Biswas, Satish Vitta, Suddhasatta Mahapatra, and Titas Dasgupta. Enhanced thermoelectric performance in mg 2 si by functionalized co-doping. *physica status solidi (a)*, 215:1700829, 07 2018.

[46] Ben hai Yu, Dong Chen, Qingbin Tang, Chunlei Wang, and Deheng Shi. Structural, electronic, elastic and thermal properties of mg2si. *Journal of Physics and Chemistry of Solids*, 71:758–763, 2010.

[47] Alain Karma. Phase-field formulation for quantitative modeling of alloy solidification. *Phys. Rev. Lett.*, 87:115701, Aug 2001.

[48] Xiaoqing Wang and Kevin Chou. Microstructure simulations of inconel 718 during selective laser melting using a phase field model. *The International Journal of Advanced Manufacturing Technology*, 100, 02 2019.

[49] Nikolas Provatas and Ken R. Elder. Phase-field methods in materials science and engineering. 2010.

[50] Wenjia Xiao, Simeng Li, Cunshan Wang, Yan Shi, Jyotirmoy Mazumder, H. Xing, and Lijun Song. Multi-scale simulation of dendrite growth for direct energy deposition of nickel-based superalloys. *Materials Design*, 164:107553, 12 2018.

[51] Jingyu Qin, Xinxin Li, Jin Wang, and Shaopeng Pan. The self-diffusion coefficients of liquid binary m-si (m=al, fe, mg and au) alloy systems by first principles molecular dynamics simulation. *AIP Advances*, 9:035328, 03 2019.

[52] Osman Kahveci, Harun Erol, Omar Joban, and Mehmet Gündüz. Determination of solid-liquid interfacial energy of solid mg2si intermetallic phase in equilibrium with liquid alsimg eutectic solution in alsimg energy storage alloy. *Intermetallics*, 135:107235, 08 2021.

[53] S. Kou and Y. H. Wang. Three-dimensional convection in laser melted pools. *Metallurgical Transactions A*, 17(12):2265–2270, December 1986.

[54] Hengji Zhang, Tao Zheng, Bruce Gnade, and Kyeongjae Cho. The effect of point defects and nanoparticles on thermal conductivity of magnesium silicide. *Computational Materials Science*, 104, 06 2015.

[55] Shuai Liu and Hanjie Guo. Balling behavior of selective laser melting (slm) magnesium alloy. *Materials*, 13:3632, 08 2020.

[56] Mohammad Yasseri, Kunal Mitra, Aryan Sankhla, Johannes de Boor, and Eckhard Müller. Influence of mg loss on the phase stability in mg2x (x = si, sn) and its correlation with coherency strain. *Acta Materialia*, 208:116737, 2021.

[57] Gagan Goyal and Titas Dasgupta. Effect of magnesium content and processing conditions on phase formation and stability in mg2+ si0.3sn0.7. *Journal of Electronic Materials*, 47, 01 2018.

[58] Gunstein Skomedal, Alexander Burkov, Alexander Samunin, Reidar Haugsrud, and Hugh Middleton. High temperature oxidation of mg2(si-sn). *Corrosion Science*, 111:325–333, 2016.

[59] Seshadev Sahoo and Kevin Chou. Phase-field simulation of microstructure evolution of ti–6al–4v in electron beam additive manufacturing process. *Additive Manufacturing*, 9:14–24, 2016.

[60] Di Wang, Shibiao Wu, Fan Fu, Shuzhen Mai, Yongqiang Yang, Yang Liu, and Changhui Song. Mechanisms and characteristics of spatter generation in slm processing and its effect on the properties. *Materials Design*, 117:121–130, 2017.

[61] Yefeng Yu, Lu Wang, Jun Zhou, Hongxin Li, Yang Li, Wentao Yan, and Feng Lin. Impact of fluid flow on the dendrite growth and the formation of new grains in additive manufacturing. *Additive Manufacturing*, 55:102832, 2022.

[62] Stephen H. Davis. *Theory of Solidification*. Cambridge Monographs on Mechanics. Cambridge University Press, 2001.

[63] W. Kurz and D.J. Fisher. Dendrite growth at the limit of stability: tip radius and spacing. *Acta Metallurgica*, 29(1):11–20, 1981.